Journal Pre-proof

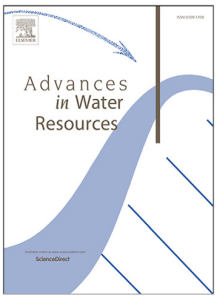

A generalized kinetic theory of Ostwald ripening in porous media

Nicolas Bueno, Luis Ayala, Yashar Mehmani

PII: S0309-1708(24)00213-6
DOI: https://doi.org/10.1016/j.advwatres.2024.104826
Reference: ADWR 104826

To appear in: *Advances in Water Resources*

Received date : 7 June 2024
Revised date : 13 September 2024
Accepted date : 20 September 2024

Please cite this article as: N. Bueno, L. Ayala and Y. Mehmani, A generalized kinetic theory of Ostwald ripening in porous media. *Advances in Water Resources* (2024), doi: https://doi.org/10.1016/j.advwatres.2024.104826.

A generalized kinetic theory of Ostwald ripening in porous media

Nicolas Bueno[a], Luis Ayala[a], Yashar Mehmani[a,*]

[a] *The Pennsylvania State University, Department of Energy and Mineral Engineering, University Park, PA, USA*

Abstract

Partially miscible bubbles (e.g., CO_2) trapped inside a porous medium and surrounded by a wetting phase (e.g., water) occur in a number of applications including underground hydrogen storage, geologic carbon sequestration, and the operation of electrochemcial devices such as fuel cells and electrolyzers. Such bubbles evolve due to a process called Ostwald ripening that is driven by differences in their interfacial curvature. For spherical bubbles, small bubbles shrink and vanish while feeding into larger ones, resulting in one large bubble at equilibrium. Within the confinement of a porous medium, however, bubbles can attain a distribution of sizes at equilibrium that have identical curvature. This work concerns itself with the formulation of a kinetic theory that predicts the statistical evolution of bubble *states*, defined as the sizes of the pores within which bubbles are trapped and the extent to which those pores are saturated with bubbles. The theory consists of a population balance equation and appropriate closure approximations. Systematic comparisons against a previously published pore network model (PNM) are conducted to validate the theory. Our theory generalizes existing variants in the literature limited to spherical bubbles trapped in homogeneous media to non-spherical (deformed) bubbles inside microstructures with arbitrary heterogeneity and spatial correlation in pore/throat sizes. We discuss the applicability, limitations, and implications of the theory towards future extensions.

Keywords: Porous media; Ostwald ripening; Bubbles; Pore scale; Pore network; Kinetic theory

1. Introduction

When partially miscible bubbles nucleate or become trapped inside a porous medium, due to fluid-fluid displacements for example, they dissolve into the surrounding wetting phase and exchange mass with each other by a process called *Ostwald ripening* [1]. If the wetting phase is quiescent with uniform pressure as assumed here, ripening is driven by differences in the interfacial curvature κ between bubbles, which shifts the local equilibrium concentration of the dissolved species in the wetting phase immediately adjacent to each bubble. The higher a bubble's curvature, thus pressure, the larger its adjacent concentration. Such differences in curvature induce concentration gradients that drive Fickian diffusion through the wetting phase. The result is the growth of some bubbles at the expense of others that shrink or dissolve completely. The implications touch many subsurface and manufacturing applications from underground hydrogen storage [2], geologic CO_2

*Corresponding author
Email address: yzm5192@psu.edu, 110 Hosler Building, University Park, PA, 16802 (Yashar Mehmani)

sequestration [3], to the optimal design of fuel cells [4] and electrolyzers [5], where the occurrence of bubbles inhibits the storage capacity and hydraulic conductivity of the porous rock (during shut-in periods) or device.

In a bulk fluid, bubbles are always spherical in shape, and ripening leads to their gradual coarsening until a single large bubble remains [6]. This is because curvature, κ, is a monotonically decreasing function of bubble volume, V^b. Hence, the smaller a bubble gets, the faster it dissolves into the surrounding fluid and vice versa. By contrast, in a porous medium, bubbles can deform due to the geometric confinement imposed by the void space. This renders the relationship between κ and V^b non-monotonic [7, 8], and thereby promotes the emergence of equilibrium states where large and small bubbles coexist with equal curvature [9, 10]. Recent theoretical work by the authors [11] has shown that the probability density function (PDF) of bubble sizes (or V^b) at equilibrium can be determined from its initial condition and the distribution of pore sizes in the porous medium. This theory was later extended from the ripening of single-component bubbles to that of multi-component bubbles [2]. What this theory *cannot* predict is the timescale over which ripening occurs and the evolution of the bubble-size PDF in time. This is precisely the subject we shall study herein.

For bubbles in a bulk fluid, the celebrated Lifshitz–Slyozov–Wagner (LSW) theory [12, 13] describes how the distribution function of bubble radii, $g(R^b)$, evolves in time during an asymptotic (self-similar) regime, established after sufficient time has elapsed from the start of ripening. The quantity $g(R^b)\,dR^b$ is the number of bubbles with radii between R^b and $R^b + dR^b$. The theory consists of the population balance equation:

$$\frac{\partial g}{\partial t} + \frac{\partial}{\partial R^b}(g u_R) = 0 \tag{1}$$

for g, where u_R is the velocity in the statistical space of R^b. The latter is computed via:

$$u_R = \frac{dR^b}{dt} \propto \frac{\sigma}{R^b}\left(\frac{1}{R^b_c} - \frac{1}{R^b}\right) \tag{2}$$

where σ is the surface tension and we have omitted the proportionality constant for clarity. The R^b_c denotes a *critical radius*, above which bubbles grow and below which bubbles shrink. A useful conceptual picture is that each bubble of radius R^b interacts with a mean field, whose equivalent bubble radius is R^b_c. Notice the curvature of spherical bubbles satisfies $\kappa = 2/R^b$ (thus $\kappa^c = 2/R^b_c$) by the Young-Laplace equation. Imposing conservation of mass, contained in bubbles and the dissolved species, as a constraint on Eq.2 yields an expression for R^b_c, which closes the theory. LSW derived an analytical expression for g and R^b_c using self-similarity arguments, assuming $g(R^b) = (R^b_c)^{-4} f(R^b/R^b_c)$ for some $f(\cdot)$, in the asymptotic regime [6].

For bubbles in a porous medium, the LSW theory was generalized by Yu et al. [14] with the key limitations that bubbles be spherical and the porous medium be homogeneous. The main modification to LSW occurred in the expression for u_R in Eq.2, which was expressed as follows:

$$\frac{dV^b}{dt} \propto \frac{A_t}{L_t}\left(\kappa^c - \kappa\right) \tag{3}$$

where L_t and A_t are, respectively, the length and cross-sectional area of throats (or pipes) that connect pores (or boxes) in a graph-based representation of the porous medium called a *pore network*. Given $V^b = 4\pi(R^b)^3/3$, $\kappa = 2/R^b$, and $\kappa^c = 2/R^b_c$ hold for spherical bubbles, the main difference between Eqs.3 and 2 is that the

pre-multiplier $1/R^b$ is replaced with the bubble-size independent quantity A_t/L_t. In other words, the porous medium imposes a fixed structure upon the *spatial arrangement* of bubbles, but does not cause deformation in their *shape*. Following steps similar to LSW, Yu et al. [14] derived a self-similar solution for g.

In this work, we propose a theory that generalizes that of [14] to porous materials with arbitrary heterogeneity and spatial correlation in pore/throat sizes and to non-spherical bubble shapes deformed by the geometric confinement of the void space. The main idea is to define g in terms of two coordinates in a statistical phase space, instead of just one (i.e., R^b). The first is the pore size, R_p, within which a bubble is confined, and the second is the fraction of the pore's volume, V_p, occupied by the bubble. The latter equals $S^b = V^b/V_p$ and is referred to as the bubble saturation. The two coordinates define the *state* of each bubble as the pair $s = (S^b, R_p)$. The population balance Eq.1 is then solved numerically on this 2D phase space, with the scalar velocity u_R replaced by a vector $\boldsymbol{u}_s$. Closure is achieved by writing an expression for $\boldsymbol{u}_s$ similar to Eq.3, but because this step requires certain approximations (to be discussed), we present two variants of our theory: (1) Theory-C, where spatial correlations in bubble states (thus pore sizes) are honored; and (2) Theory-U, where such correlations are neglected. We validate Theory-C and -U systematically against an existing pore network model (PNM) [11] and show both perform well in uncorrelated microstructures but only Theory-C performs well in correlated ones. We then highlight the limitations of Theory-C and discuss directions for future research. Chief among the shortcomings are the requirements that each bubble be confined to only one pore and the initial configuration of bubbles in a *correlated* microstructure not be overly sparse.

We note that recent work on Ostwald ripening of bubbles in porous media has undergone rapid developments that includes an increasing array of experimental observations [9, 15–17], computational modeling via PNMs [2, 8, 10, 11, 18] and level-set methods [19–21], and theoretical formulations geared towards statistical [2, 14, 22] and macroscopic [23–27] descriptions of the physics. These works provide valuable and robust frameworks within which the proposed theory herein can be validated and extended further in the future.

The paper's outline is as follows: In Section 2, we describe the conceptual problem to be solved. Section 3 reviews the PNM by [11] used here to validate Theory-C/U and provide a mathematical basis for their formulation. We next present Theory-C/U in Section 4, starting with definitions and the guiding hypothesis, followed by the governing equations and closure approximations. Section 5 outlines the problem set chosen to validate the two theories against the PNM in Section 6. Lastly, we discuss the applicability, limitations, and implications of Theory-C/U in Section 7 and conclude with a summary of key takeaways in Section 8.

2. Problem description

We conceptualize a porous microstructure with a network (or graph) of interconnected *pores* linked via narrower channels called *throats*, as shown in Fig.1. The dimensions of both may be spatially heterogeneous and/or correlated. All pores and throats are filled with a continuous, but stagnant (non-flowing), wetting phase (e.g., water). Some pores are occupied by a single-component, perfectly non-wetting (contact angle of 180^o), and incompressible bubble or droplet (e.g., $scCO_2$). The placement of bubbles is often determined

by fluid-fluid displacements that precede entrapment, such as cyclic injections in underground hydrogen storage [28]. We assume, for the sake of simplicity, that each bubble occupies no more than one pore. All bubbles are partially miscible in the wetting phase and in local equilibrium with the solution adjacent to their interface. Since bubbles have different sizes, thus interfacial curvatures, they will be at equilibrium with fluids of different concentration. The induced concentration gradient drives molecular diffusion and thereby mass exchange between bubbles, a process known as *Ostwald ripening*. Our goal is formulate a theory that predicts the evolution kinetics of an initial bubble population in a statistical sense. Concretely, we aim to quantify how the joint distribution of bubble sizes and occupied pores evolves in time. This allows estimating the timescale of ripening and its final equilibrium state. Existing theories are limited to predicting either the kinetics for spherical bubbles inside homogeneous media [14] or equilibrium states alone (no kinetics) [2].

In Section 3, we first review the pore-network model (PNM) by Mehmani & Xu [11] that simulates Ostwald ripening of bubbles within arbitrary pore networks under the assumptions stated above. The PNM's governing equations provide a basis to formulate the theory in Section 4 and validate it in Section 6. The theory, though solved numerically, achieves orders of magnitude ($\times 10^{3-4}$) of speedup in computational cost compared to the PNM and allows for the effective parameterization of upscaled (or Darcy) models [27]. Finally, while both the PNM and the proposed theory apply to networks with arbitrary geometric and topological complexity, all simulations herein are conducted on 2D lattice networks comprised of 3D pore/throat shapes.

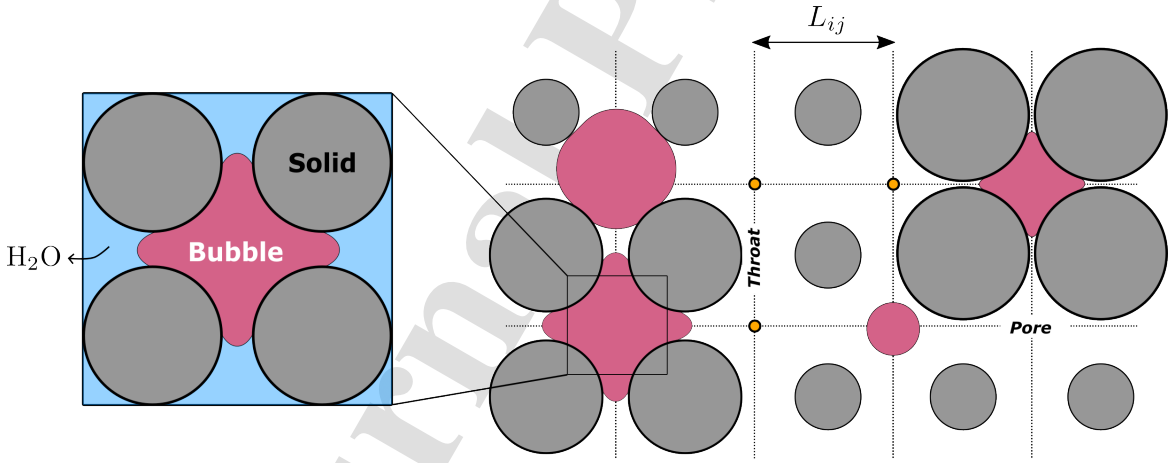

Figure 1: Conceptualization of a porous microstructure by a computational graph or pore network, consisting of local geometric enlargements called *pores* linked via geometric bottlenecks called *throats*. The pores and throats are filled with a continuous but stagnant (non-flowing) wetting phase (e.g., H_2O), with some pores also occupied by a partially miscible and perfectly non-wetting (contact angle of 180^o) bubble (e.g., $scCO_2$). The bubbles dissolve and exchange mass through Ostwald ripening.

3. Pore network model (PNM)

Consider a partially miscible bubble occupying pore i in a pore network, that is connected to z_i neighboring pores. The conservation of mass for such a bubble can be written as follows [2, 11]:

$$\frac{dn_i}{dt} = \sum_{j=1}^{z_i} J_{ij} = \sum_{j=1}^{z_i} \frac{D_m A_{ij}}{v_w L_{ij}} (x_j - x_i) \tag{4}$$

where n_i is the bubble's number of moles,[1] J_{ij} the diffusive flowrate between pores i and j, D_m the molecular diffusion coefficient of the dissolved species, v_w the molar volume of the bulk wetting phase, and x_i and x_j the concentrations of the dissolved species in units of mole fraction in pores i and j. The A_{ij} and L_{ij} denote the cross-sectional area and length of throat ij connecting pores i and j, respectively. Eq.4 embeds Fick's law, which assumes that dissolved concentrations are dilute. Since bubbles are assumed incompressible in Section 2, they have constant molar volume v_b. Thus, the accumulation term in Eq.4 can be expressed as:

$$\frac{1}{v_b} \frac{dV_i^b}{dt} = \sum_{j=1}^{z_i} \frac{D_m A_{ij}}{v_w L_{ij}} (x_j - x_i) \tag{5}$$

where V_i^b is the volume of the bubble in pore i.

To close Eq.5, and to be able to solve it in terms of solute concentrations as the primary unknowns, we need two constitutive equations that relate V_i^b to x_i. The first is the expression of thermodynamic equilibrium between the dissolved concentration x_i and the interfacial curvature κ_i of the bubble in pore i [23]:

$$\ln \frac{x_i}{x_o} = \frac{\sigma \kappa_i v_b}{RT} \tag{6}$$

In Eq.6, x_o is a reference taken to be the equilibrium concentration for a flat interface. The parameters σ, R, and T denote interfacial tension, universal gas constant, and temperature, respectively (all constants here).

The second constitutive equation we need expresses the dependence between κ_i and V_i^b, dictated by a bubble's size and geometric deformation of its shape due to confinement, as shown in Fig.2. This dependence is non-monotonic and exhibits a characteristic U-shape [7, 9] captured by the following equation:

$$\kappa_i = \kappa_i(V_i^b, V_{p,i}) = \begin{cases} \kappa_i^{min} \left(\dfrac{V_{c,i}}{V_i^b} \right)^{\frac{1}{3}} & \text{if} \quad V_i^b < V_{c,i} \\ \kappa_i^{min} \left(1 + a \dfrac{V_i^b - V_{c,i}}{V_{p,i} - V_{c,i}} + b \dfrac{V_i^b - V_{c,i}}{V_{p,i} - V_i^b} \right) & \text{if} \quad V_i^b \geq V_{c,i} \end{cases} \tag{7}$$

Eq.7 was proposed by [8] for ("semi-")cubic pores with a side-half length of $R_{p,i}$. Such a pore has a volume of $V_{p,i} = (2R_{p,i})^3$ and a maximally inscribed sphere of radius $R_{p,i}$ and volume $V_{c,i} = 4\pi R_{p,i}^3/3$. The $\kappa_i^{min} = 2/R_{p,i}$ denotes the curvature of the inscribed sphere, and a and b are empirical parameters (here $a = 1$ and $b = 0.01$). Notice Eq.7 consists of two branches. If $V_i^b < V_{c,i}$, the bubble is spherical and does not touch the pore's walls,

[1] The PNM actually treats n_i as the *total* number of moles in pore i, accounting for the amount in the bubble plus that dissolved in the wetting phase. We have omitted the dissolved contribution from the presentation here merely to simplify the formulation of our theory later, and because its magnitude is relatively small. See also the discussion in Section 6.4 of [11].

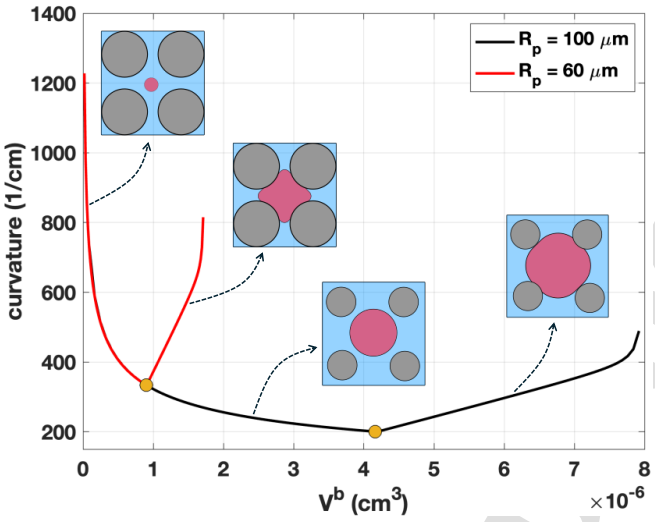

Figure 2: Schematic of the characteristic U-shaped dependence between a bubble's interfacial curvature, κ, and it volume, V^b, when confined within a pore. Curves for two pore sizes are plotted via Eq.7. Each consists of a sub- and a super-critical branch, separated by the critical volume, V_c (yellow dots). The sub-critical branches overlap, as they correspond to spherical bubbles. Insets show that bubbles on the super-critical branch are deformed to different degrees in small (red) and large (black) pores.

whereas if $V_i^b > V_{c,i}$, the bubble is non-spherical and is deformed by the pore geometry (see Fig.2). We refer to V_{c_i} as the pore's *critical volume*, and denote any bubble that satisfies $V_i^b < V_{c,i}$ as being *sub-critical* and any bubble satisfying $V_i^b > V_{c,i}$ as *super-critical*. We also note that in single-component ripening, sub-critical bubbles are unstable because a small reduction in their size increases their capillary pressure, and with it, their dissolution rate. This means that if one of two identical bubbles is perturbed in size, the system is knocked out of equilibrium and the smaller bubble disappears. By contrast, super-critical bubbles are stable and may equilibrate with other bubbles that have different shapes and sizes [7, 10], i.e., small perturbations to equilibrated bubble sizes attenuate instead of amplifying. Fig.2 shows that the curvature κ_i of a super-critical bubble depends not only on its volume V_i^b but also on the confining pore's size $V_{p,i}$ (or equivalently $R_{p,i}$). Coupling Eq.5 with Eqs.6-7 yields a nonlinear system of equations in terms of the pore concentrations x_i, which we solve with a modified Newton scheme detailed in [11]. The solver is equipped with adaptive time stepping capabilities to capture rapid early-time and slow late-time dynamics of ripening. If pore i does *not* contain a bubble, the left-hand side of Eq.5 simplifies to $(V_{p_i}/v_w)dx_i/dt$, obtained from dn_i^w/dt and $n_i^w = x_i V_{p_i}/v_w$ where n_i^w is the number of dissolved moles in pore i. As a result, Eqs.6-7 are no longer needed. An extension of the above PNM to multi-component, compressible gas bubbles was proposed in [2].

4. Ripening theory

4.1. Definitions and guiding hypotheses

We formulate a theory that predicts the temporal evolution in the statistics of an initial bubble population trapped inside a porous medium with arbitrary pore-size distribution (PSD) and spatial correlation. The

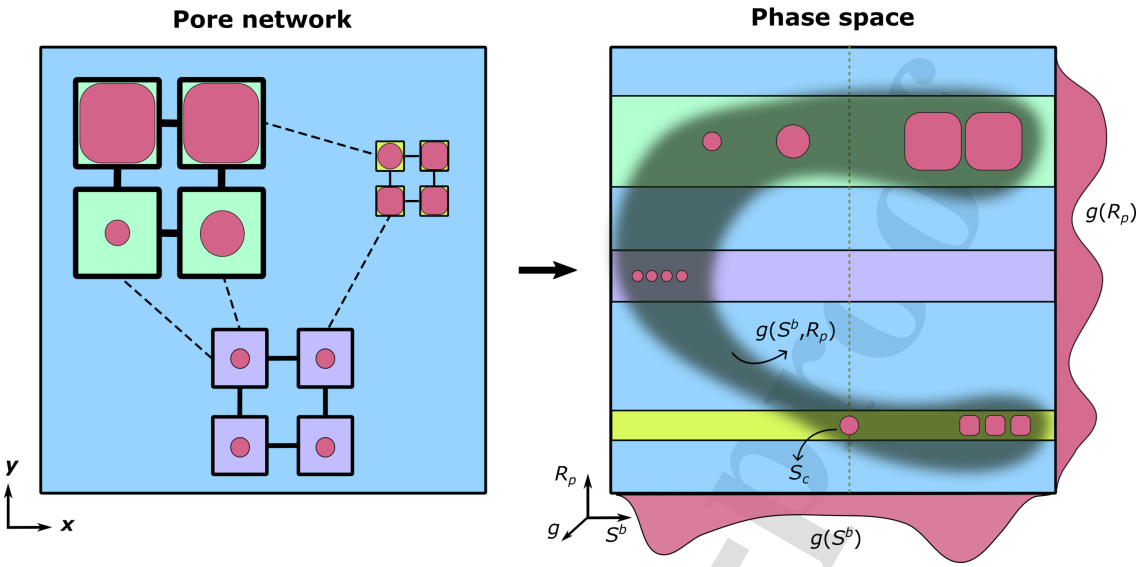

Figure 3: (Left) Spatial representation of bubbles with different volumes V^b trapped inside a pore network with pore sizes R_p. (Right) Statistical representation of the bubbles in a phase space defined by S^b- and R_p-axes. Bubbles in this phase space are identified by their state, $s=(S^b, R_p)$, and their number is quantified by the distribution function $g(s;t)$ (shaded area). The 1D distribution functions plotted along the bottom and right borders (pink) represent the marginal distributions of $g(s;t)$. The bubble sizes and color codes used for pores in the left panel are mapped and honored in the panel to the right. Notice one of the bubbles coincides with the maximally inscribed sphere in its yellow-colored pore, and thus has critical saturation $S_c=V_c/V_p$.

evolution is driven entirely by Ostwald ripening. Specifically, and with reference to the left panel of Fig.3, we consider a pore network that has different pore sizes, R_p, containing an initial distribution of bubble volumes, V^b. Since ripening is driven by gradients in bubble curvature, and curvature depends on V^b and R_p through Eq.7, we define a bubble's *state* as the point $s=(V^b, R_p)$ in a 2D statistical *phase space* with V^b- and R_p-axes. Equivalently, and to simplify later analysis, we denote bubble states via $s=(S^b, R_p)$, where $S^b=V^b/V_p$ is the occupied pore's bubble saturation (recall $V_p=8R_p^3$). The right panel of Fig.3 shows the phase space in terms of the S^b- and R_p-axes. We now introduce $g(S^b, R_p; t)$ as the distribution function of bubbles defined over this phase space, such that the quantity $g(S^b, R_p; t)\, dS^b dR_p$ denotes the number of bubbles residing in pores that have sizes between R_p and $R_p + dR_p$ and filled to saturations between S^b and $S^b + dS^b$ at time t. Our goal is to compute $g(S^b, R_p; t)$ at all t using information available only at $t=0$, including $g(S^b, R_p; 0)$ and the spatial statistics of pore occupancy. For brevity, we shall refer to the foregoing joint distribution function as $g(s;t)$, where the semicolon emphasizes that t is a parameter, not a random variable.

By replacing the *spatial* evolution problem of bubbles (left in Fig.3) with their *statistical* evolution (right in Fig.3), we circumvent the need for tracking individual bubbles as is done in the PNM. Instead, we track bubble *states* shared among many bubbles, leading to dramatic speedup and upscaling. Specifically, the cost of theoretical calculations does not depend on the domain size and number of bubbles in it, unlike PNM. The success in formulating such an ensemble description hinges upon two guiding hypotheses: (1) the network

is sufficiently large for spatial and ensemble statistics to have converged; and (2) bubbles in state s interact with a *mean field*, that in turn dictates how $g(s;t)$ should evolve. This mean field is defined in the following sections. First, we propose a population balance equation for $g(s;t)$ in Section 4.2 that is advected in phase space via the velocity $\boldsymbol{u}_s$. We then derive an explicit expression for $\boldsymbol{u}_s$ in Section 4.3. The proposed theory generalizes the LSW theory for bubbles in bulk fluids [12, 13], and that of [14] for sub-critical bubbles in homogeneous porous media, to arbitrarily shaped bubbles in heterogeneous and correlated porous media.

4.2. Population balance equation

Let $\Omega(t)$ represent a closed region in the interior of the phase space in Fig.3. The integral of $g(s;t)$ over $\Omega(t)$ denotes the *number* (not probability or fraction) of bubbles that have states within Ω. As bubbles evolve due to Ostwald ripening, so does $\Omega(t)$, provided we keep track of the bubbles contained in it. So long as $\Omega(t)$ remains within the interior of the phase space, and does not intersect the $S^b=0$ axis, the integral of $g(s;t)$ over $\Omega(t)$ is a conserved quantity and, therefore, the Reynolds transport theorem yields:

$$\frac{d}{dt}\int_{\Omega(t)} g(s,t)\,d\Omega = 0 \qquad \Rightarrow \qquad \frac{\partial g}{\partial t} + \nabla\cdot(g\boldsymbol{u}_s) = \frac{\partial g}{\partial t} + \frac{\partial}{\partial S^b}(g u_{S^b}) + \frac{\partial}{\partial R_p}(g u_{R_p}) = 0 \tag{8}$$

where $\boldsymbol{u}_s = (u_{S^b}, u_{R_p})$ is the velocity with which bubbles in state s move through the phase space. Note the integral of $g(s;t)$ over the whole phase space (i.e., number of *all* bubbles) is *not* conserved, because bubbles can vanish during ripening by dissolving completely. When a bubble is in the process of vanishing, its volume, thus saturation, undergoes $S^b \to 0$. Hence, if such a bubble is within $\Omega(t)$, the boundary of $\Omega(t)$ intersects the $S^b=0$ axis. This is why Eq.8 holds strictly in the *interior* (not axes) of the phase space. We call Eq.8 the *population balance equation* and solve it numerically on a Cartesian grid that discretizes the phase space.

The state velocity $\boldsymbol{u}_s$ has two components $u_{S^b} = dS^b/dt$ and $u_{R_p} = dR_p/dt$. Given our assumption in Section 2 that bubbles are confined to only one pore each, and our further postulate here that bubbles do not undergo hydrodynamic mobilization during ripening, $u_{R_p}=0$ must hold. These assumptions are consistent with our PNM. That said, in many systems, bubbles do span multiple pores and can indeed mobilize between pores [8]. However, we defer these complexities to future extensions of the theory in the interest of keeping the scope focused. With the $u_{R_p}=0$ simplification, Eq.8 decouples into a series of 1D equations for each fixed R_p. Since Eq.8 is hyperbolic, we use a first-order upwind scheme with respect to u_{S^b} to discretize it. Given Eq.8 is also first-order, we only need one boundary condition (BC). In Section 2, we assumed that bubbles span only one pore, so no bubbles can enter or exit the domain close to the $S^b=1$ boundary of the phase space. Due to the specific form of Eq.7 chosen, which possesses a vertical asymptote at $S^b=1$ (i.e., $\kappa\to\infty$), we are guaranteed (as seen later) that the horizontal component of the phase velocity points leftward (specifically $u_{S^b}\to-\infty$ as $S^b\to1$). The implication is that to enforce a no-flux BC, it suffices to impose $g\to0$ as $S^b\to1$. The $S^b=0$ boundary of the phase space is open to outflux of g, as bubbles can vanish, so no BC is needed. We next turn our attention to deriving an expression for $\boldsymbol{u}_s=(u_{S^b},\,0)$, or equivalently dS^b/dt.

4.3. Mean-field approximation

Here, we formulate an expression for dS_s^b/dt, which determines the advective velocity $\boldsymbol{u}_s = (dS_s^b/dt,\ 0)$ for the distribution function $g(s;t)$ in phase space (Fig.3). The subscript s in dS_s^b/dt specifies the velocity belongs to state s. We begin by reformulating Eq.5 of the PNM, and assume for the time being that all z_i neighboring pores are occupied by a bubble. We shall revisit and remove this latter assumption in a Remark stated at the end of this section. Since $x_i/x_o \approx 1$ holds in practice [13], Eq.6 can be linearized as:

$$x_i \approx x_o\left(1 + \frac{\sigma\kappa_i v_b}{RT}\right) \tag{9}$$

Then, substituting Eq.9 for x_i and x_j into Eq.5, and using $S_i^b = V_i^b/V_{p,i}$, we obtain:

$$\frac{dS_i^b}{dt} = \frac{1}{V_{p,i}}\sum_{j=1}^{z_i}\frac{v_b^2 D_m \sigma x_o}{v_w RT}\frac{A_{ij}}{L_{ij}}(\kappa_j - \kappa_i) = \frac{C}{V_{p,i}}\sum_{j=1}^{z_i}\frac{A_{ij}}{L_{ij}}(\kappa_j - \kappa_i) \tag{10}$$

where $C = (v_b^2 D_m \sigma x_o)/(v_w RT)$ is a constant.

Now let I_s denote the index set of all bubbles with state s. Namely, bubbles in I_s reside in pores that have a size $R_{p,s}$ and filled to a saturation S_s^b. If n_s is the number of members in I_s, we define the state average as:

$$(\cdot)_s = \frac{1}{n_s}\sum_{i\in \mathrm{I}_s}(\cdot)_i \tag{11}$$

Operating Eq.11 on both sides of Eq.10, and noticing $S_i^b = S_s^b$, $\kappa_i = \kappa_s$, and $V_{p,i} = V_{p,s}\ \forall i \in \mathrm{I}_s$, we get:

$$\frac{dS_s^b}{dt} = \frac{C}{V_{p,s} n_s}\sum_{i\in \mathrm{I}_s}\sum_{j=1}^{z_i}\frac{A_{ij}}{L_{ij}}(\kappa_j - \kappa_s) \tag{12}$$

To make further progress, we must express the right-hand side of Eq.12 in terms of the neighboring bubble *states* s', not *pores* j. This requires the introduction of a conditional probability $p(s'|s;t)$, which quantifies the likelihood that a bubble in an adjacent pore is in state s' given the current bubble is in state s. Moreover, average, or mean-field, properties must be assigned to bubbles and throats in each state. These include z_s, $A_{ss'}$, and $L_{ss'}$, denoting the average number of bubbles adjacent to a bubble in state s, and the cross-sectional area and length of a throat connecting bubbles in states s and s', respectively. With these probabilistic definitions in place, we can now write the following identity:

$$\frac{1}{n_s}\sum_{i\in \mathrm{I}_s}\sum_{j=1}^{z_i}\frac{A_{ij}}{L_{ij}}(\kappa_j - \kappa_s) = z_s\int_{s'} p(s'|s;t)\frac{A_{ss'}}{L_{ss'}}(\kappa_{s'} - \kappa_s)\, d\Omega \tag{13}$$

where the integral runs over all neighboring states s' in phase space.

Substituting Eq.13 into Eq.12, followed by some algebraic manipulation, yields our final expression:

$$\frac{dS_s^b}{dt} = \frac{C z_s}{V_{p,s}}\left(\frac{A}{L}\right)_s(\kappa_s^c - \kappa_s) \tag{14a}$$

where

$$\kappa_s^c = \left(\frac{A}{L}\right)_s^{-1}\int_{s'} p(s'|s;t)\frac{A_{ss'}}{L_{ss'}}\kappa_{s'}\, d\Omega\,, \qquad \left(\frac{A}{L}\right)_s = \int_{s'} p(s'|s;t)\frac{A_{ss'}}{L_{ss'}}\, d\Omega \tag{14b}$$

Notice Eq.14a is similar to the LSW relations in Eqs.2-3, except that it accounts for the spatial heterogeneity and correlation induced by a confining pore space. Specifically, the conditional probability $p(s'|s;t)$ is high when bubbles in states s and s' are proximate neighbors, but low otherwise. This is the case if pores with radii R_p and R'_p are physically connected to each other via throats; recall $s=(S^b, R_p)$ and $s'=(S'^b, R'_p)$. In Eq.14a, k_s^c is the *mean-field curvature* with which all bubbles in state s exchange mass. Notice bubbles in each state interact with a different mean field or k_s^c. Eq.14 is the most general form of our theory, providing the sought-after $\boldsymbol{u}_s=(dS_s^b/dt, 0)$ for the population balance Eq.8. But unfortunately, Eq.14 is also the most cumbersome form as its numerical solution requires $p(s'|s;t)$, a 4D array that must be stored and updated as $g(s;t)$ evolves. These tasks can be memory intensive and difficult to ensure computational tractability.

We therefore introduce two approximations to Eq.14 in the next sections, which lead to two simplified variants of our theory: *Theory-C* and *Theory-U*, where suffixes C and U stand for "correlated" and "uncorrelated." Theory-C accounts for spatial correlations, like Eq.14, but reduces the 4D array $p(s'|s;t)$ to the 2D array $p(R'_p|R_p;t)$. Theory-U goes one step further and ignores all spatial correlations altogether, resulting in the replacement of $p(R'_p|R_p;t)$ with the 1D probability density function (PDF) $p(R'_p;t)$.

Remark. In deriving Eq.14a from Eq.12, we assumed the coordination number z_s (or z_i) represents the number of *bubble-occupied* pores connected to bubble s (or pore i). This poses a problem because if all neighboring pores of a bubble are empty, its saturation will cease to evolve (i.e., $dS_s^b/dt=0$). But this cannot be, given bubble s can still exchange mass with distant bubbles two or more pores away. The rigorous way to address the shortcoming would be to account for such high-order interactions via $p(s'|s;t)$, but this is rather difficult as discussed in Section 7 and beyond our scope. A partial remedy adopted here is to reinterpret z_s as the coordination number of the pore network, i.e., the number of neighboring pores connected to bubble s *irrespective of whether they contain a bubble*. This ensures bubble s continues to exchange mass with the mean field through all of its throats, as long as at least one of its neighboring pores remains occupied.

4.4. Theory-C: preserving spatial correlations

We begin formulating Theory-C by simplifying the joint probability $p(s'|s;t)$ as follows:

$$p(s'|s;t) \approx p(s'|R_p;t) = p(S'^b, R'_p|R_p;t) = p(R'_p|R_p;t)\, p(S'^b|R'_p, R_p;t) \approx p(R'_p|R_p;t)\, p(S'^b|R'_p;t) \qquad (15)$$

where we have assumed $p(s'|s;t) \approx p(s'|R_p;t)$ and $p(S'^b|R'_p, R_p;t) \approx p(S'^b|R'_p;t)$. The first approximation means that a neighboring bubble's state s' depends chiefly on the current bubble's *pore size* and not so much on the size of the current bubble itself. In other words, spatial correlations are assumed to arise mainly from the structure of the pore network, rather than from differences in bubble saturation. While artificial counter examples violating this assumption can be easily conjured, in practice, the initial configuration of bubbles in a porous medium is determined by trapping processes that follow fluid displacements and precede ripening. Such trappings are heavily influenced by the pore-network structure. The second approximation has a parallel

meaning, namely, the probability of finding a bubble with saturation (or volume) S'^b is controlled more by the size of its confining pore R'_p and less by the size of its neighboring pore R_p.

In addition to Eq.15, we postulate the following identities:

$$A_{ss'} \approx A_{R_pR'_p}, \qquad L_{ss'} \approx L_{R_pR'_p}, \qquad z_s \approx z_{R_p} \tag{16}$$

which are reasonable because the cross-sectional area and length of a throat depend less on the volumes (or saturations) of the two bubbles straddling it, and more on the sizes of the pores linked by the throat. Similarly, the coordination number of a bubble at state s is dictated mainly by the size of the pore confining it, and less by the size of the bubble itself. Notice $A_{R_pR'_p}$ and $L_{R_pR'_p}$ represent statistical averages, because even after fixing R_p and R'_p, the areas and lengths of the throats connecting such pore sizes exhibit distributions. Likewise, z_{R_p} is an ensemble average because fixing R_p does not guarantee a fixed coordination number.

Armed with Eqs.15 and 16, we can now simplify Eq.14 as follows:

$$\frac{dS^b_s}{dt} = \frac{Cz_{R_p}}{V_{p,s}} \left(\frac{A}{L}\right)_s (\kappa^c_s - \kappa_s) \tag{17a}$$

where

$$\kappa^c_s = \left(\frac{A}{L}\right)^{-1}_s \int_{R'_p} p(R'_p|R_p;t) \frac{A_{R_pR'_p}}{L_{R_pR'_p}} \bar{\kappa}_{R'_p} dR'_p\,, \qquad \left(\frac{A}{L}\right)_s = \int_{R'_p} p(R'_p|R_p;t) \frac{A_{R_pR'_p}}{L_{R_pR'_p}} dR'_p \tag{17b}$$

$$\bar{\kappa}_{R'_p} = \int_{S'^b} p(S'^b|R'_p;t)\, \kappa_{s'} dS'^b\,, \qquad p(S'^b|R'_p;t) = g(S'^b|R'_p;t) \left(\int_{S'^b} g(S'^b|R'_p;t) dS'^b\right)^{-1} \tag{17c}$$

The detailed derivations of Eqs.17b-c are given in Appendix A. Notice $\bar{\kappa}_{R'_p}$ is the average curvature of bubbles that occupy pores with size R'_p, which depends on $p(S'^b|R'_p;t)$. The latter is computed from $g(s;t)$ via the right expression in Eq.17c. The conditional probability $p(R'_p|R_p;t)$ poses some challenges. For a given pore network occupied by bubbles at $t=0$, we can easily calculate $p(R'_p|R_p;0)$ from the spatial information provided. But as bubbles evolve into later times, such spatial statistics is no longer available in our theory, because only $g(s;t)$ is solved by the population balance Eq.8. Yet, we must update $p(R'_p|R_p;t)$, as it captures spatial correlations in the *bubble-occupied* portion of the network, which is time dependent.

In Appendix B, we show that if $p(R'_p|R_p;0)$ is known, $p(R'_p|R_p;t)$ can be readily computed via:

$$p(R'_p|R_p;t) = \frac{f_{R'_p}\, p(R'_p|R_p;0)}{\int_{R'_p} f_{R'_p}\, p(R'_p|R_p;0)\, dR'_p}\,, \qquad f_{R'_p} = \frac{g(R'_p;t)}{g(R'_p;0)}\,, \qquad g(R'_p;t) = \int_{S'^b} g(S'^b, R'_p;t) dS'^b \tag{18}$$

In practice, $p(R'_p|R_p;t)$ and $g(S^b, R_p;t)$ are stored as matrices in computer memory and updated at each time step that the population balance Eq.8 is evolved. In this format, Eq.18 is equivalent to performing a series of row/column-scalings of the $p(R'_p|R_p;t)$ matrix, and row/column-sums of the $g(S^b, R_p;t)$ matrix.

To summarize, Theory-C consists of computing dS^b_s/dt via Eq.17a, where κ^c_s and $(A/L)_s$ are approximated via Eqs.17b-c and 18. First, $p(R'_p|R_p;0)$ is calculated from the spatial distribution of bubbles at $t=0$, which is assumed to be known, and $A_{R_pR'_p}$, $L_{R_pR'_p}$, and z_{R_p} are obtained from the spatial statistics of the network itself. At any later time t, as the population balance Eq.8 has been evolved to yield $g(s;t)$, Eq.18 is used to compute $p(R'_p|R_p;t)$. Substituting the latter into Eq.17 allows updating the phase velocity $\boldsymbol{u}_s = (dS^b_s/dt, 0)$

at all s in phase space. Finally, by inserting $\boldsymbol{u}_s$ back into Eq.8, we can evolve $g(s;t)$ to the next time step. Note that the evolutions of $g(s;t)$ and $p(R'_p|R_p;t)$ in time impact both $(A/L)_s$ and κ^c_s in Eq.17a.

4.5. Theory-U: neglecting spatial correlations

Theory-C requires the storage of matrices for $p(R'_p|R_p;t)$ and $A_{R_pR'_p}/L_{R_pR'_p}$, with the former updated via Eq.18 through time. Theory-U simplifies the formulation by reducing these quantities into 1D vectors. The starting point is the assumption that all spatial correlations can be neglected, leading to:

$$p(R'_p|R_p;t) \approx p(R'_p;t) \tag{19}$$

Moreover, the following approximation is introduced:

$$\frac{A_{R_pR'_p}}{L_{R_pR'_p}} \approx \left(\frac{A}{L}\right)_{R_p} := \int_{R'_p} p(R'_p;0)\frac{A_{R_pR'_p}}{L_{R_pR'_p}}\,dR'_p \approx \left(\frac{A}{L}\right)_s \tag{20}$$

where the second equality is a definition that assigns to each pore size R_p an average value $(A/L)_{R_p}$.

Given Eqs.19 and 20, we can now simplify κ^c_s in Eq.17 as follows:

$$\kappa^c_s = \int_{R'_p} p(R'_p;t)\,\bar{\kappa}_{R'_p}\,dR'_p = \int_{s'} p(s';t)\,\kappa_{s'}\,d\Omega := \kappa^c \tag{21}$$

Notice κ^c_s does not depend on the bubble state s, hence we have renamed it to κ^c. This means in Theory-U, all bubbles interact with a *single mean field*. The expression for $\bar{\kappa}_{R'_p}$ remains the same as Eq.17c and the expression for dS^b_s/dt is the same as Eq.17a. The second equality in Eq.21 results from substituting $\bar{\kappa}_{R'_p}$ and using $\int_{s'} d\Omega = \int_{R'_p}\int_{S'^b} dS'^b dR'_p$. The PDF $p(s';t)$ is equal to $g(s';t)/n_b$, where n_b is the number of bubbles at time t, defined below. Notice the mean-field curvature κ^c in Theory-U equals the *mean curvature* computed over the entire phase space; not so for κ^c_s in Theory-C. The nuanced part again is computing $p(R'_p;t)$.

In Appendix C, we show that if $p(R'_p;0)$ is known, $p(R'_p;t)$ can be computed via:

$$p(R'_p;t) = \frac{f_{R'_p}\,p(R'_p;0)}{F}, \qquad F = \frac{n_b}{n^0_b}, \qquad n_b = \int_s g(s;t)\,d\Omega, \qquad n^0_b = \int_s g(s;0)\,d\Omega \tag{22}$$

where n_b and n^0_b are the total number of bubbles in the pore space at the current and initial times, respectively, and F is the fraction of the surviving bubbles at any given time during Ostwald ripening. The quantity $f_{R'_p}$ was defined in Eq.18. In Appendix C, we show that $p(R'_p;0)$ can be computed from $g(s;0)$ via:

$$p(R'_p;0) = \frac{g(R'_p;0)}{n^0_b} \tag{23}$$

where $g(R'_p;0)$ was defined in Eq.18. Note that Eq.23, and Theory-U as a whole, does not require *any* spatial information about the size or occupancy of bubbles in the pore network at $t=0$, unlike Theory-C.

4.6. Summary of the solution procedure

Suppose an initial distribution of bubbles in phase space, $g(s;0)$, and their corresponding spatial distribution in a pore network are given. The latter is needed only in Theory-C. We execute the following steps in

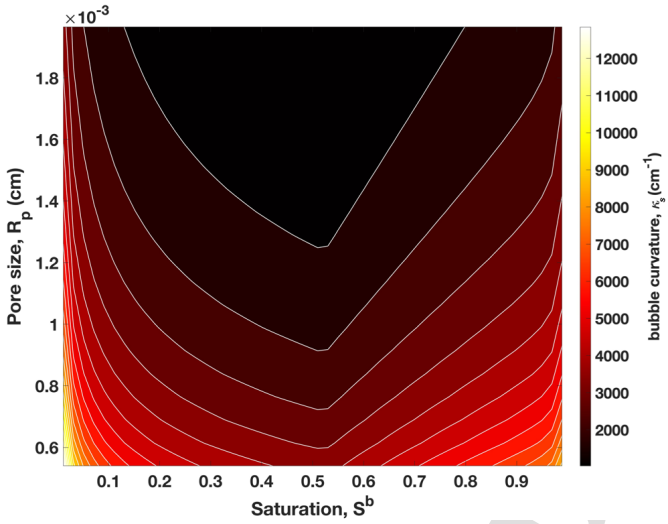

Figure 4: The distribution and contour lines of bubble curvatures, κ_s, in phase space computed via Eq.7. Dark colors correspond to low curvatures, where bubble saturations are near their critical values ($S_c = V_c/V_p = \pi/6$) and/or pore sizes are larger.

order: (1) Compute $p(R_p'|R_p;0)$ from the spatial information for Theory-C and compute $p(R_p';0)$ via Eq.23 for Theory-U; (2) Calculate κ_s for every point in phase space using Eq.7, a visualization of which is given in Fig.4; (3) Use these to obtain κ_s^c via Eq.17b for Theory-C and κ^c via Eq.21 for Theory-U; (4) Compute dS_s^b/dt via Eq.17a for Theory-C and Theory-U (use Eqs.20-21 for the latter), then insert in $\boldsymbol{u}_s = (dS_s^b/dt, 0)$ to yield the phase velocity for the population balance Eq.8; (5) Discretize Eq.8 via a 1D finite volume method subject to the BC discussed in Section 4.2, then advance by one time step to obtain $g(s;t)$; (6) Update $p(R_p'|R_p;t)$ and $p(R_p';t)$ via Eqs.18 and 22 for Theory-C and Theory-U, respectively; (7) Repeat from Step 3.

5. Validation set

We validate Theory-C and -U against PNM simulations on pore networks that have different levels of heterogeneity and spatial correlation in pore sizes, and are occupied by bubbles with different spatial configuration and total initial saturation S_t^b. We use S_t^b to denote the total saturation in a network and to differentiate it from S^b used to denote the saturation of a single bubble inside a pore. The PNM presented in Section 3 has been validated itself against microfluidic experiments [11]. With reference to Fig.5, we consider four pore-network types: (1) *homogeneous*, with a single pore size; (2) *patterned*, comprised of only two pore sizes; (3) *heterogeneous but spatially uncorrelated* pore sizes; and (4) *heterogeneous and spatially correlated* pore sizes. The patterned networks themselves divide into 4×4, 8×8, and 16×16 arrangements of small and large pores as shown in Fig.5. All networks are topologically 2D lattices made of a 50×50 array of pores. Thus, the coordination number of all pores is $z_i = 4$, except for boundary pores where the value is less.

We define the *heterogeneity ratio* as $R_{het} = R_{p,max}/R_{p,min}$, where $R_{p,max}$ and $R_{p,min}$ are the maximum and minimum pore sizes in the network, respectively. For the homogeneous network, $R_{het} = 1$. All patterned networks have $R_{het} = 4$. For the remaining heterogeneous networks, we draw R_p from a uniform distribution

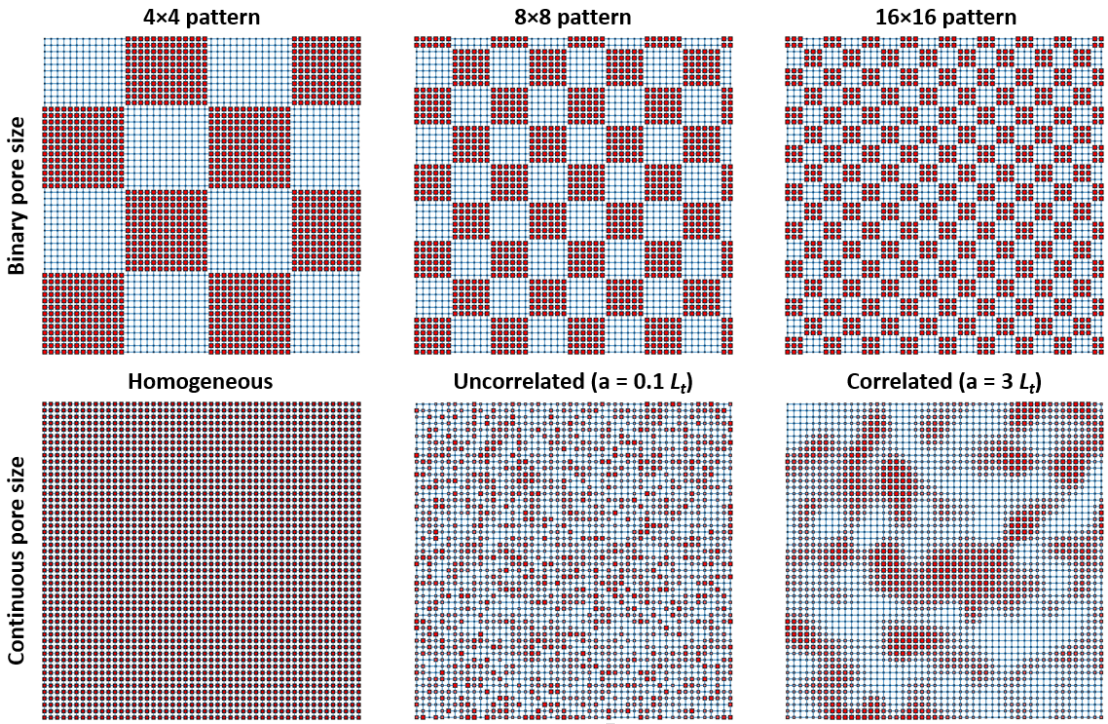

Figure 5: Pore networks used to validate Theory-C/U. Top row: Patterned networks comprised of two pore sizes. They decrease in spatial correlation from left to right. Bottom row: Networks with homogeneous, heterogeneous but spatially uncorrelated, and heterogeneous and spatially correlated pore sizes drawn from a continuous distribution. All networks are 50×50 lattices.

between $R_{p,min}$ and $R_{p,max}$, or $\mathcal{U}(R_{p,min}, R_{p,max})$, and consider $R_{het}=4$ and 8. To create spatially correlated networks, we first generate a random Gaussian field $\xi \sim \mathcal{N}(\mu, C(h))$ with mean $\mu=0$ and covariance function:

$$C(h) = \exp\left(\frac{h}{a}\right) \tag{24}$$

where a is the correlation length and h the distance between any two pores. The field consists of an array of random numbers, ξ, defined at the pore centers. Notice Eq.24 entails a unit variance at $h=0$. We then map ξ, which can take on negative values, onto the uniform pore-size distribution $\mathcal{U}$ using the *inverse probability integral transform* method. Namely, we compute $R_p = F_U^{-1}(F_{\mathcal{N}}(\xi))$, where F_N and F_U are the cummulative distribution functions of $\mathcal{N}$ and $\mathcal{U}$, respectively. We consider $a = 0.1L_t$ and $3L_t$, where L_t is the lattice spacing (i.e., throat length). The former yields a spatially uncorrelated network, and the latter a correlated network, both illustrated in Fig.5. When varying R_{het} between 4 and 8, we keep the generated ξ field fixed, and only change the distribution function $\mathcal{U}$. In other words, the only difference between $R_{het}=4$ and 8 for a fixed a lies in the contrast between the pore sizes, not their relative spatial arrangements.

The above cases amount to a total of 8 networks, consisting of 1 homogeneous, 3 patterned, 2 heterogeneous uncorrelated, and 2 heterogeneous correlated. For each, we consider two initial bubble saturations $S_t^b=30\%$ and 60%; for the homogeneous network we also probe 7.5% to allow comparison against an existing theory [14]. Table 1 summarizes these cases and establishes a shorthand for referencing them. For homoge-

Table 1: Validation set used to compare Theory-C and -U against the PNM. It consists of homogeneous, patterned, heterogeneous uncorrelated, and heterogeneous correlated pore networks that are filled initially with bubbles up to different total saturations.

Description	Correlation length (a)	R_{het}	S_t^b	Name
Homogeneous, very low S_t^b	-	1	7.5%	Ho-S08
Homogeneous, low S_t^b	-	1	30%	Ho-S30
Homogeneous, high S_t^b	-	1	60%	Ho-S60
Patterned, 4×4	$13L_t$	4	60%	Pt-4
Patterned, 8×8	$6L_t$	4	60%	Pt-8
Patterned, 16×16	$3L_t$	4	60%	Pt-16
Low R_{het}, uncorrelated, low S_t^b	$0.1L_t$	4	30%	R4-Unc-S30
Low R_{het}, uncorrelated, high S_t^b	$0.1L_t$	4	60%	R4-Unc-S60
Low R_{het}, correlated, low S_t^b	$3L_t$	4	30%	R4-Cor-S30
Low R_{het}, correlated, high S_t^b	$3L_t$	4	60%	R4-Cor-S60
High R_{het}, uncorrelated, low S_t^b	$0.1L_t$	8	30%	R8-Unc-S30
High R_{het}, uncorrelated, high S_t^b	$0.1L_t$	8	60%	R8-Unc-S60
High R_{het}, correlated, low S_t^b	$3L_t$	8	30%	R8-Cor-S30
High R_{het}, correlated, high S_t^b	$3L_t$	8	60%	R8-Cor-S60
Complex bubble placement, uncorrelated	$0.1L_t$	4	32%	Cmplx-Unc
Complex bubble placement, correlated	$3L_t$	4	32%	Cmplx-Cor
Same as Cmplx-Unc except with variable A_t/L_t	$0.1L_t$	4	32%	vAL-Unc
Same as Cmplx-Cor except with variable A_t/L_t	$3L_t$	4	32%	vAL-Cor

neous networks, we use Ho-S30, for example, to denote S_t^b=30%. For patterned networks, we use Pt-4, Pt-8, and Pt-16 to denote the 4×4, 8×8, and 16×16 patterns in Fig.5. For other heterogeneous networks, we use R8-Cor-S60, for example, to denote $R_{het}=8$, correlated pore sizes with $a=3L_t$, and an initial bubble saturation of S_t^b=60%. As another example, R4-Unc-S30 means $R_{het}=4$, uncorrelated pore sizes with $a=0.1L_t$, and S_t^b=30%. Unless stated otherwise, most networks are initialized by placing a bubble in all pores with the local $S^b=V^b/V_p$ equaling the global S_t^b. Finally, we consider two additional cases denoted by Cmplx-Unc and Cmplx-Cor in Table 1, whose pore networks are identical to R4-Unc and R4-Cor, respectively, except the initial placement of bubbles is much more complex (described later).

The validations in Section 6 are organized according to the horizontal groupings of the cases in Table 1, which increase systematically in level of complexity. First, we focus on homogeneous networks, and compare predictions from Theory-C/U against the PNM and an existing theory by Yu et al. [14]. Since the latter is valid for very low (sub-critical) bubble saturations, we set S_t^b=7.5%. We also probe S_t^b=30% and 60% for

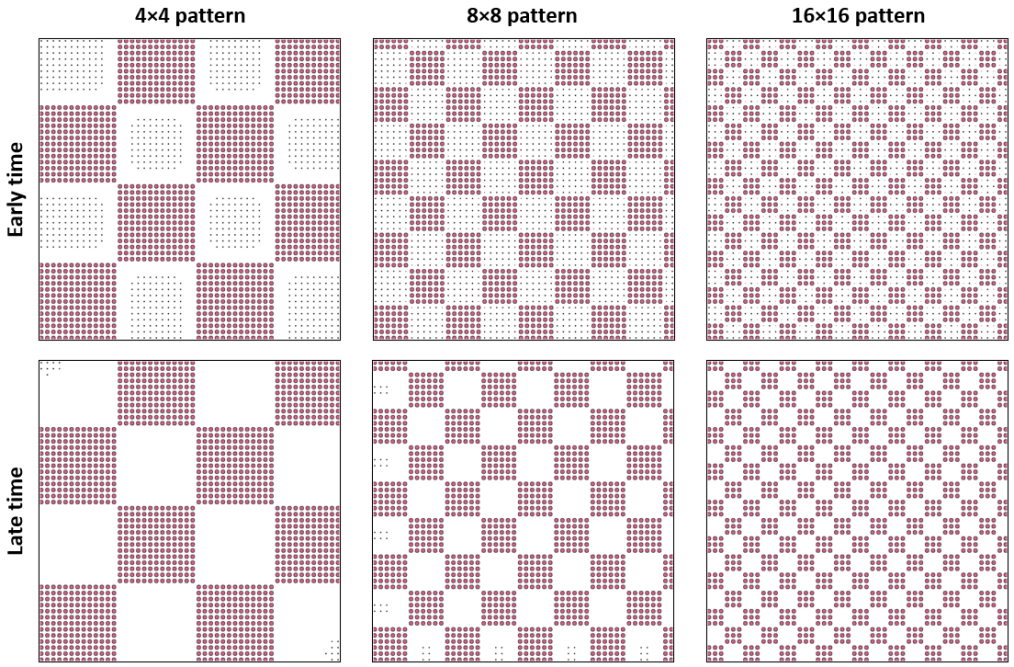

Figure 6: PNM predictions of early- and late-time spatial distributions of bubbles due to ripening in the patterned networks of Fig.5, corresponding to the Pt-4, Pt-8, and Pt-16 cases in Table 1. Bubbles are depicted by circles whose radii are proportional to the bubbles' sizes. Snapshots are taken at times 10 and $100hr$ for Pt-4, 1 and $10hr$ for Pt-8, and 1 and $10hr$ for Pt-16.

which the existing theory is not valid. Next, we consider patterned networks made from two pore sizes whose spatial correlations increase progressively from Pt-16 to Pt-8, then Pt-4. After that, we validate Theory-C/U against more complex heterogeneous networks, whose pore sizes are drawn from uniform distributions and spatial correlations are induced via Eq.24. Next, we focus on the impact of complex initial bubble placements within the most heterogeneous networks from the previous grouping in Table 1. In all the above cases, the ratio A_t/L_t for all throats (cross-sectional area over length) is kept uniform to probe the sole impact of bubble states (pore size and bubble saturation) on ripening dynamics. The final grouping in Table 1 introduces the added complexity of having a variable A_t/L_t in the networks from the prior grouping. In all validations that follow, no parameter tuning of any sort is performed for Theory-C or -U, i.e., all predictions are blind.

To guide the discussion, Figs.6 and 7 depict early- and late-time spatial distributions of bubbles obtained via PNM for the Ho-S30, Pt-4, Pt-8, Pt-16, R4-Unc-S60, and R4-Cor-S60 networks in Table 1. This subset is representative of all other cases in Table 1. For simplicity, each bubble is depicted by a circle whose radius is proportional to the bubble's size. Notice small bubbles initially in small pores (Fig.5) shrink and eventually vanish during ripening, with their mass transferring to bubbles in larger pores. Our goal with Theory-C/U is to predict the statistical distribution function $g(s;t)$ obtained numerically from the PNM. The latter informs us of what bubble sizes reside in which pores. In all cases, the constant C in Eq.10 is $3.553\times10^{-13}cc/s$.

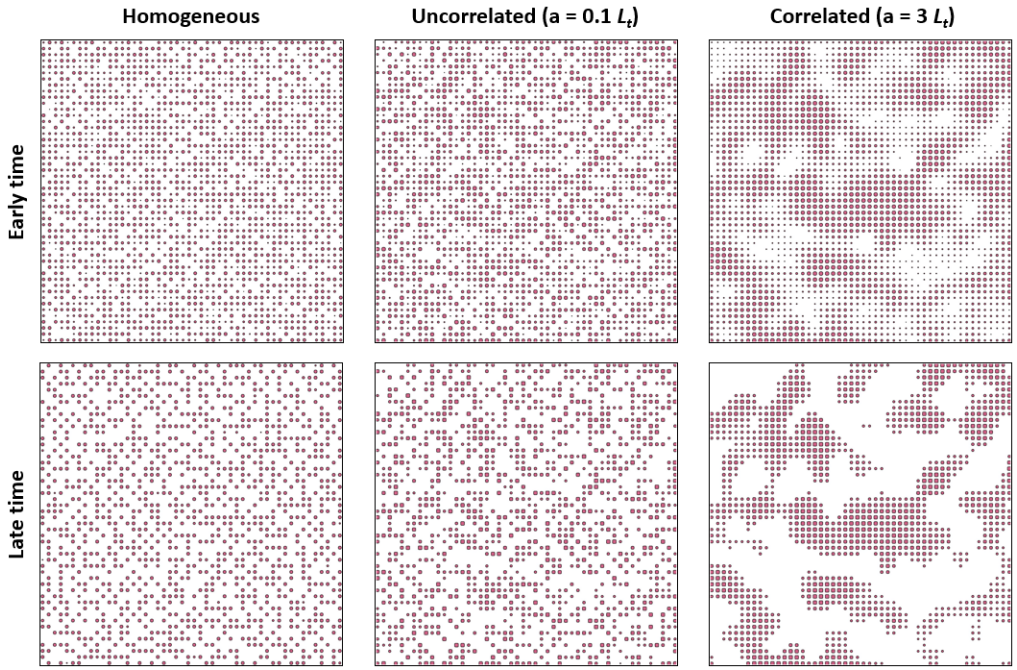

Figure 7: PNM predictions of early- and late-time spatial distributions of bubbles in the homogeneous and heterogeneous networks of Fig.5, i.e., Ho-S30, R4-Unc-S60, and R4-Cor-S60 in Table 1. Bubbles are depicted by circles with radii proportional to their sizes. Snapshots are at times 0.1 and $1hr$ for Ho-S30, 10 and 10^3hr for R4-Unc-S60, and 10 and 10^4hr for R4-Cor-S60.

6. Results

6.1. Comparison against existing theory: spherical bubbles

Here, we compare Theory-C and -U against the PNM of Section 3 and an existing theory by Yu et al. [14]. Since the theory of [14] is valid when all bubbles are spherical (or sub-critical), we use the low-saturation Ho-S08 network in Table 1. The network is homogeneous with a pore size of $R_p = 5\mu m$, a throat length of $L_t = 10\mu m$, and a throat cross-sectional area of $A_t = 19.6\mu m^2$. To trigger the onset of ripening, as sub-critical bubbles are unstable, we perturb the bubble saturations in each pore by initializing them randomly between 5% and 10%. At early to moderate times, when bubbles are still spherical with radius R^b, their curvatures can be computed via $\kappa = 2/R^b$. But at late times, some bubbles become deformed by the pore walls, hence their curvatures depend on the bubble volumes according to Eq.7. To enable one-to-one comparison against the sub-critical theory of [14], we transform super-critical bubble volumes (or saturations) obtained from the PNM and Theory-C/U to R^b by replacing them with a sphere of the same volume. The latter is done through a post-processing step, not during simulations or analytical calculations. In Yu et al.'s theory, each bubble interacts with a mean field that is represented by a virtual bubble of radius R^b_c, called the *critical radius*. This is similar to the mean-field curvatures κ^c_s and κ^c in Theory-C and -U, respectively. Notice in a homogeneous network, the distribution function $g(S^b, R_p; t)$ depends only on S^b, and Eqs.17b and 21 simplify to yield $\kappa^c_s = \kappa^c$. At early to moderate times, when all bubbles are spherical, $R^b_c = 2/\kappa^c$. But at late times,

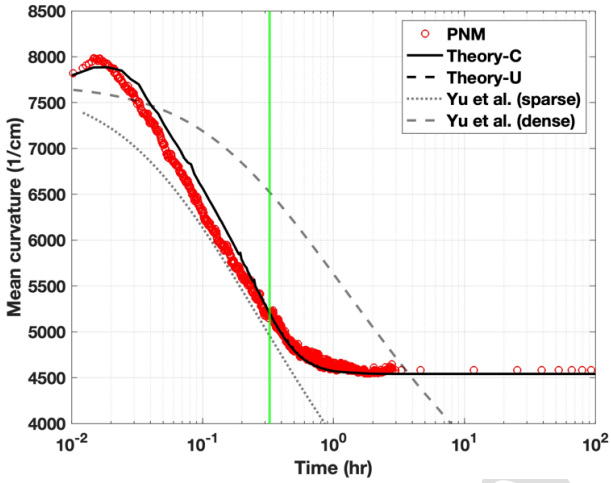

Figure 8: Comparison of the evolution of the mean bubble curvature ($=2/R_c^b$) through time predicted by the PNM in Section 3, Theory-C and -U in Section 4, and an existing theory by Yu et al. [14] for spherical (or sub-critical) bubbles. The latter consists of predictions for "sparse" and "dense" spatial configurations of bubbles. The curves for Theory-C and -U overlap perfectly. The vertical green line marks the first time a bubble touches its pore's walls, after which the theory by [14] is no longer valid.

we set R_c^b to be the harmonic mean of all volume-equivalent R^b to allow one-to-one comparison with [14].

Yu et al. showed that, except for very early times, the ripening of sub-critical bubbles reaches an asymptotic regime where R_c^b scales as $t^{1/4}$ provided the spatial arrangement of bubbles is sparse, and as $t^{2/11}$ if the arrangement is dense.[2] These apply to topologically 2D networks like the ones herein. Both scalings are plotted in Fig.8 alongside PNM simulations (used as a reference) and predictions via Theory-C/U. For consistency with results in later sections, the y-axis in Fig.8 is expressed in terms of mean curvature or $2/R_c^b$. We see that Theory-C and -U yield identical results that are in excellent agreement with PNM. In contrast, the theory by [14] agrees with the PNM only during intermediate times between 0.1 and $1hr$, when the asymptotic regime is dominant. Moreover, only the *sparse* limit of Yu et al.'s theory agrees with the PNM, most likely because many sub-critical bubbles dissolve within $0.1hr$ of ripening leading to large inter-bubble distances. At $\sim 1hr$ from the start of ripening, marked by the vertical green line in Fig.8, the first bubble in the network touches its pore's walls. After this time, not all bubbles are spherical and the theory of [14] deviates significantly. Theory-C/U, however, capture this super-critical ripening regime accurately.

Yu et al. also showed that the PDF of R^b/R_c^b is stationary (or time-independent) during the asymptotic ripening regime. This is plotted in Fig.9 and compared against the PNM simulations at three times: $0.01hr$, $0.1hr$, and $1hr$. We remark that, unlike Fig.8, the stationary PDF of [14] does not depend on whether the spatial arrangement of bubbles is sparse or dense. We see that a good agreement between Yu et al.'s theory

[2] If bubbles were gaseous satisfying the ideal gas law $v_b = RT/p^b$ and Henry's law $p^b = Hx_o$, where p^b is the bubble pressure and H is Henry's constant, then the constant in Eq.10 becomes $C = (v_b D_m \sigma)/(v_w H)$. This constant is used in the theory by [14], except it seems to have been mistakenly multiplied by x_o therein, which we have corrected in Section 6.1.

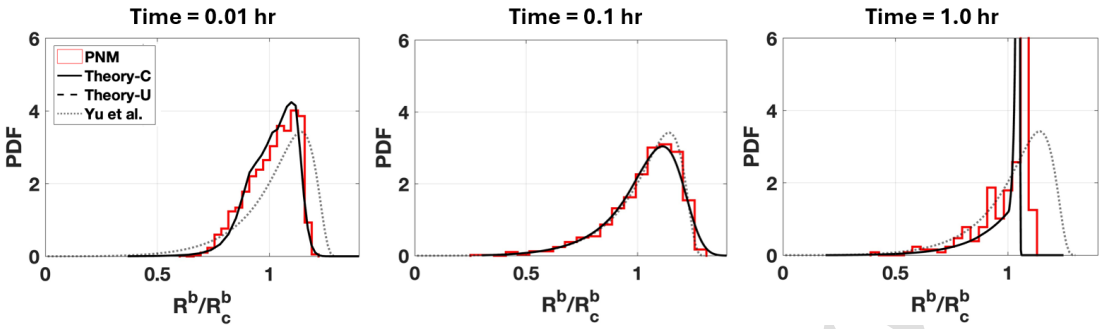

Figure 9: Comparison of PDFs of normalized bubble sizes versus time predicted by the PNM in Section 3, Theory-C and -U in Section 4, and the theory of Yu et al. [14] for sub-critical bubbles. Super-critical bubble sizes from the PNM and Theory-C/U in the $1hr$ snapshot were obtained by computing volume-equivalent sphere radii. Normalization of R^b is done against the critical radius R^b_c. The theory by [14] agrees with the PNM at $0.1hr$, after asymptotic regime has been established and before bubbles touch the pore walls. At $0.01hr$ and $1hr$, agreement is poor but captured well by Theory-C and -U, which overlap one another.

and the PNM is observed only at $0.1hr$, namely, after the asymptotic regime has been established but before any bubbles have touched their pores' walls. By contrast, Theory-C/U are in excellent agreement with the PNM for the entire duration of ripening. We thus conclude that Theory-C/U successfully generalize the theory by [14] from spherical bubbles in the asymptotic regime, to arbitrarily shaped bubbles in all regimes.

6.2. Homogeneous network at higher saturations: beyond existing theory

We next go beyond the theory of [14] and consider the same homogeneous network as in Section 6.1 but at higher bubble saturations: S^b_t=30% and 60% corresponding to the Ho-S30 and Ho-S60 cases in Table 1, respectively. In Ho-S30, local bubble saturations in pores ($=V^b/V_p$) are initialized randomly between 10%–50%, and in Ho-S60 between 30%–90%. Notice for local saturations $>\pi/6\approx 52\%$ (specific to the semi-cubic pores herein), bubbles are super-critical and non-spherical in shape. In Fig.10, we compare predictions from Theory-C/U and the PNM with respect to the mean curvature $\bar{\kappa}$, average bubble volume $\bar{V^b}$, and the fraction of survived bubbles F defined in Eq.22 versus time. For reasons stated in Section 6.1, Theory-C and -U yield identical results within the homogeneous network, and thus only the former is depicted in Fig.10.

Fig.10 shows that Theory-C is in good agreement with the PNM for both low and high bubble saturations. When S^b_t=30%, most bubbles are initially sub-critical but become super-critical at late times; at which only 50% of the bubbles survive. This is similar to the ultra-low saturation (S^b_t=7.5%) case of Section 6.1 as depicted in Fig.8. Except here, the transient spike in $\bar{\kappa}$ at very early times is more pronounced than in Fig.8. The spike is due to a rapid decrease in the sizes of many sub-critical bubbles prior to their complete dissolution, after which $\bar{\kappa}$ declines steadily. The effect is stronger when bubbles are larger initially (S^b_t=30% here versus 7.5% in Section 6.1) because then curvatures have a lower starting point, thus a steeper climb. By contrast, when S^b_t=60%, most bubbles are initially super-critical and remain so well into late times; at which 97.5% of bubbles survive. In this case, changes in the average volume and survived fraction of bubbles are understandably small, as seen in Fig.10. But there is a sizable decline in $\bar{\kappa}$ that is captured well by Theory-C.

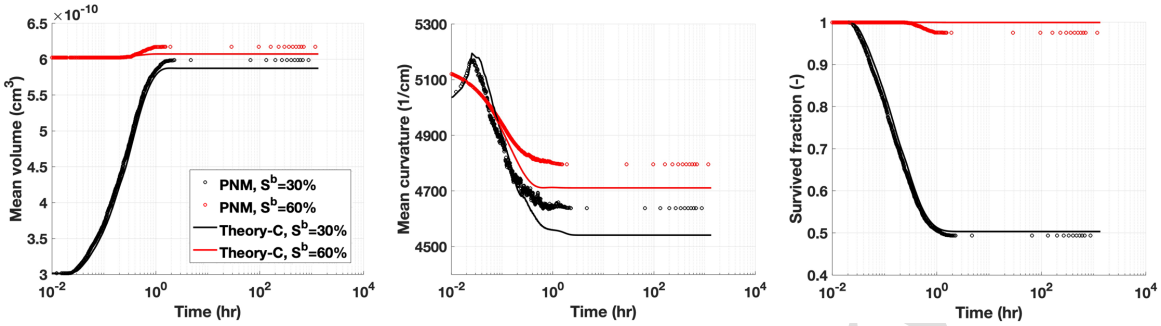

Figure 10: Comparison between Theory-C and the PNM with respect to mean curvature $\bar{\kappa}$, average bubble volume $\bar{V}^b$, and the fraction of survived bubbles F versus time in the Ho-S30 and Ho-S60 networks of Table 1. The predictions from Theory-U are omitted because they overlap with the results of Theory-C.

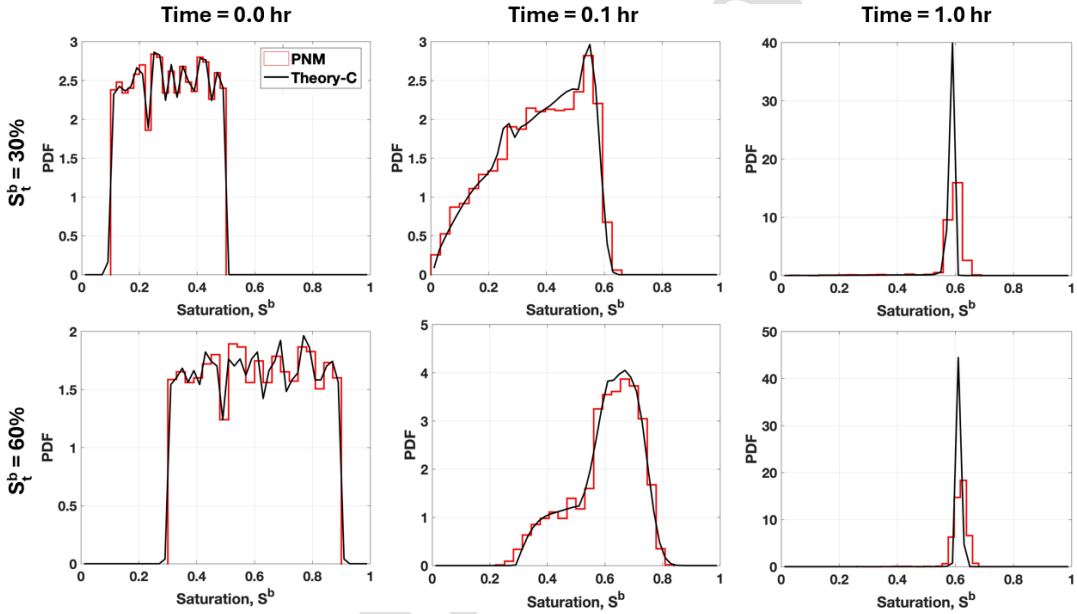

Figure 11: Comparison of PDFs of local bubble saturation in pores predicted by the PNM and Theory-C at three times (0, 0.1, and 1.0hr) and two saturations (S_t^b =30% and 60%) in the Ho-S30 and Ho-S60 networks. Theory-U overlaps with Theory-C and is thus omitted. These PDFs are different from those predicted by the asymptotic theory of [14] in Fig.9 for ultra-low S_t^b.

The origin of the slight deviations in the late-time values of $\bar{\kappa}$ (and $\bar{V}^b$ & F) are discussed in Section 7.

Fig.11 further shows the corresponding PDFs of the local bubble saturations in pores at three times. We see that Theory-C, and the overlapping Theory-U omitted, are in good agreement with the PNM. Notice the PDFs are very different from the asymptotic-regime PDFs obtained from the theory of [14] in Fig.9.

6.3. Heterogeneous networks with patterned microstructure

We now increase the level of complexity in our validation by considering the patterned networks Pt-4, Pt-8, and Pt-16 in Table 1, which consist of two pore sizes (with contrast $R_{het}=4$) arranged spatially according to Fig.5. The initial S_t^b in all three networks is 60%, which matches the local saturation in each pore. From

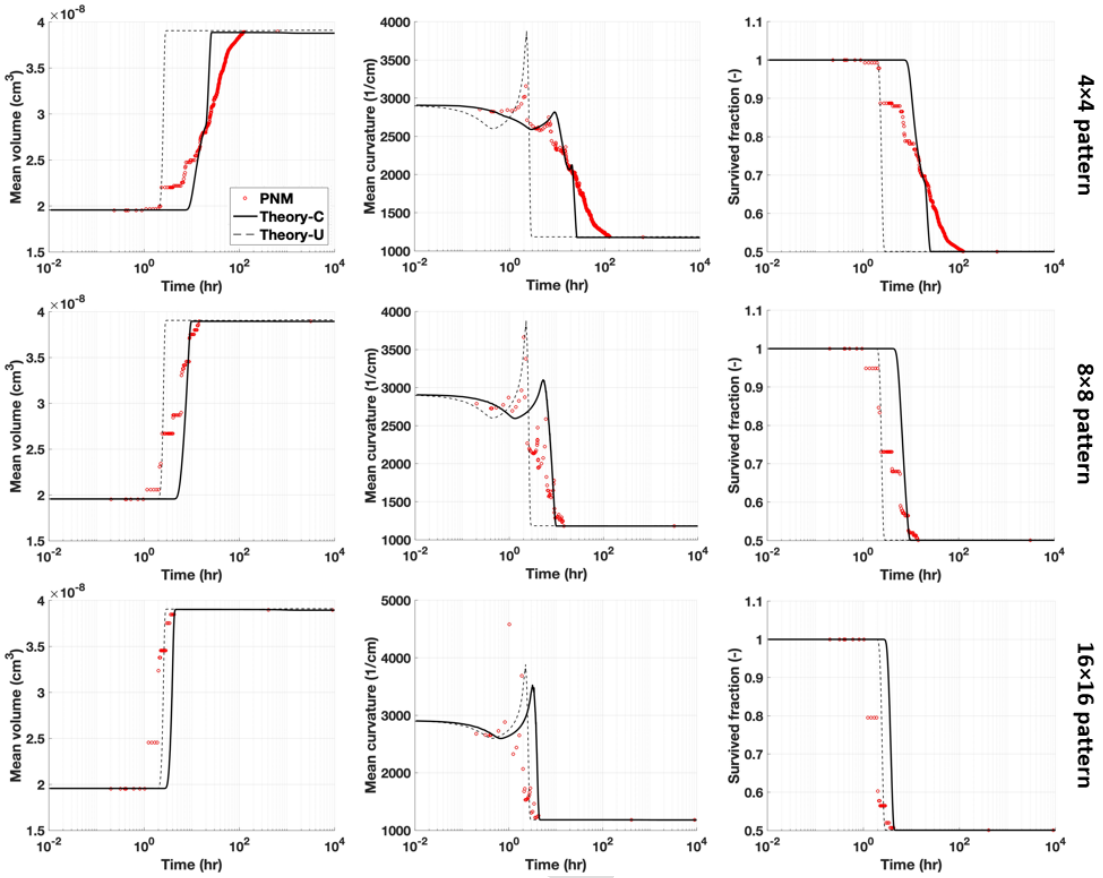

Figure 12: Comparison of (left column) mean bubble volume, (middle column) mean bubble curvature, and (right column) the fraction of survived bubbles versus time in the patterned networks Pt-4, Pt-8, and Pt-16 of Table 1 obtained via Theory-C, Theory-U, and the PNM. Spatial correlation decreases from Pt-4 to Pt-16, during which Theory-C asymptotes to Theory-U.

Fig.5 and Table 1, the correlation lengths of the networks decrease systematically from Pt-4, to Pt-8, then Pt-16. This allows testing whether spatial correlations captured via Theory-C are important, or if they can be neglected via the simpler Theory-U. Fig.12 illustrates the mean curvature $\bar{\kappa}$, mean bubble volume $\bar{V^b}$, and the fraction of survived bubbles F versus time obtained from Theory-C, Theory-U, and the PNM. Notice the mean curvature $\bar{\kappa}$ entails the average of κ_s over the entire phase space ($=\int_s \kappa_s g(s;t)\, d\Omega/n^b$) in Theory-C/U, or the spatial average of κ_i over the network in the PNM. In a heterogeneous network, like the ones here and hereafter, $\bar{\kappa}$ is different from the mean-field curvature κ_s^c in Theory-C, but equal to the κ^c in Theory-U. In a homogeneous network, like the ones considered in the previous two sections, $\bar{\kappa}=\kappa_s^c=\kappa^c$ holds.

Fig.12 shows Theory-C is in satisfactory agreement with the PNM for all correlation lengths, whereas Theory-U agrees well only at a low correlation length (Pt-16). This is expected as Theory-U neglects spatial correlations in bubble states (including pore sizes) as its central assumption. Also expected is the observation that the predictions from Theory-C asymptote to those of Theory-U in going from Pt-4 to Pt-16. Given the networks are ordered and consist of only two pore sizes, the PDFs of local bubble saturation in pores

corresponding Fig.12 are difficult to interpret and convey redundant information with respect to Fig.12. We have thus included such plots in Appendix D, where we again find satisfactory agreement between Theory-C and the PNM in all networks, and Theory-U and the PNM in the low-correlation network Pt-16 only.

6.4. Heterogeneous networks with random microstructure

We increase the difficulty of the validation further by considering the heterogeneous networks with uniform pore-size distribution in Table 1, namely, R4-Unc-S30, R4-Unc-S60, R4-Cor-S30, R4-Cor-S60, R8-Unc-S30, R8-Unc-S60, R8-Cor-S30, and R8-Cor-S60. These consist of continuous pore sizes that are spatially correlated (Cor) or uncorrelated (Unc), have low (R4: $R_{het}=4$) or high (R8: $R_{het}=8$) contrast, and are occupied by bubbles up to an initially low (S30: $S_t^b=30\%$) or high (S60: $S_t^b=60\%$) total saturation. At $t=0$, a bubble is placed in all pores with a local saturation S^b $(=V^b/V_p)$ equal to S_t^b. Figs.13 and 14 show the evolutions of the mean curvature $\bar{\kappa}$, mean bubble volume $\bar{V^b}$, and the fraction of survived bubbles F in these networks computed via Theory-C, Theory-U, and the PNM. Fig.13 depicts the results for $S_t^b=30\%$, and Fig.14 for $S_t^b=60\%$. Theory-U yields identical results for correlated and uncorrelated networks, thus only one is plotted.

We see that Theory-C is in very good agreement with the PNM in *all* networks, whereas Theory-U agrees with the PNM in uncorrelated networks only. Specifically, the application of Theory-U to correlated networks (red) is seen to result in very large errors. As expected, Theory-C reduces to Theory-U in the uncorrelated

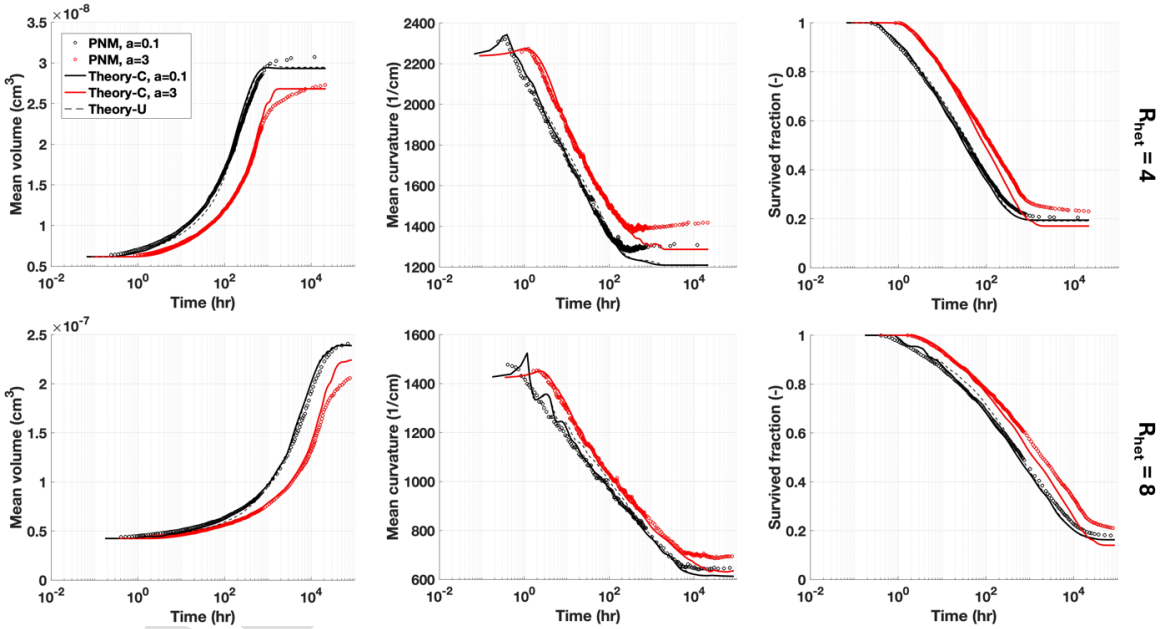

Figure 13: Comparison of (left column) mean bubble volume, (middle column) mean bubble curvature, and (right column) the fraction of survived bubbles versus time in the heterogeneous networks R4-Unc-S30, R4-Cor-S30, R8-Unc-S30, and R8-Cor-S30 computed via Theory-C, Theory-U, and the PNM. The networks include correlated (red), uncorrelated (black), low-contrast (top row), and high-contrast (bottom row) pore sizes drawn from a uniform distribution. Initial bubble saturation is $S_t^b=30\%$ in all cases. Theory-U yields identical results for correlated and uncorrelated networks, thus only one curve is plotted.

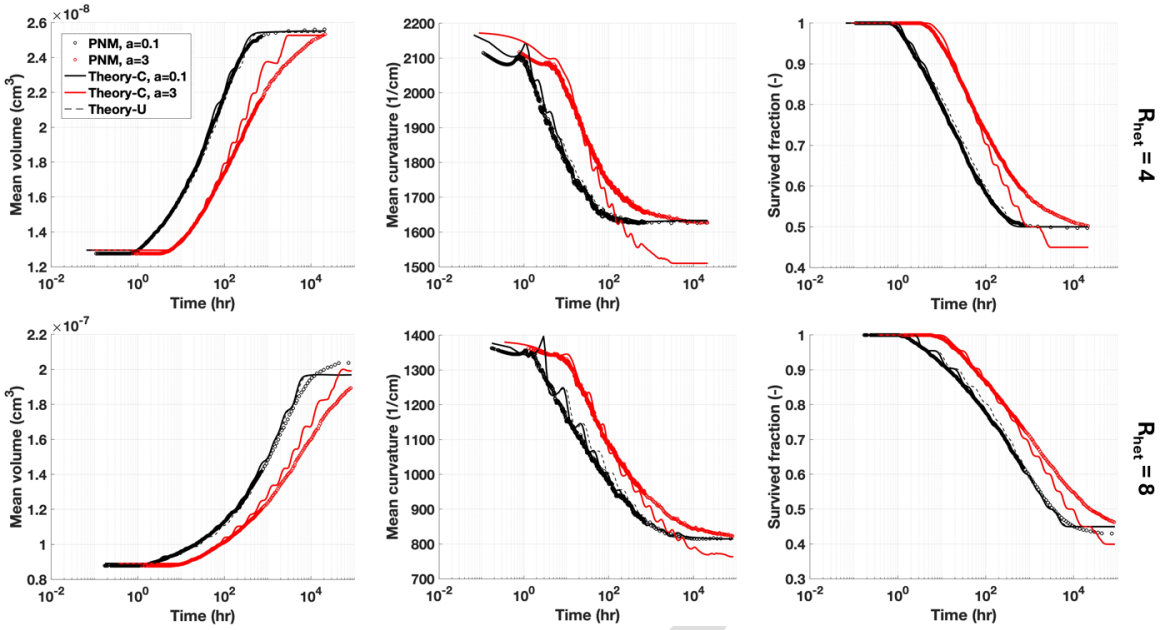

Figure 14: Comparison of (left column) mean bubble volume, (middle column) mean bubble curvature, and (right column) the fraction of survived bubbles versus time in the heterogeneous networks R4-Unc-S60, R4-Cor-S60, R8-Unc-S60, and R8-Cor-S60 computed via Theory-C, Theory-U, and the PNM. The networks include correlated (red), uncorrelated (black), low-contrast (top row), and high-contrast (bottom row) pore sizes drawn from a uniform distribution. Initial bubble saturation is S_t^b=60% in all cases. Theory-U yields identical results for correlated and uncorrelated networks, thus only one curve is plotted.

networks. Notice from Figs.13-14 that ripening is much faster in uncorrelated networks than in correlated networks. This is because larger correlation lengths in pore size entail smaller spatial gradients in bubble curvature, which ultimately drive ripening. Similar to Fig.10, we observe in Figs.13-14 deviations in $\bar{\kappa}$ at late times computed via Theory-C versus the PNM. We discuss the underlying causes for this in Section 7.

Let us now examine the PDFs of the bubble states. Since both R_p and S^b are continuous variables in the pore networks considered, we compare the distribution function $g(s;t)$ in the 2D phase space $s=(S^b, R_p)$ computed via Theory-C/U and the PNM. For brevity, we focus on the uncorrelated R4-Unc-S60 and the correlated R4-Cor-S60 networks, as all others yield similar results. Fig.15 shows three snapshots of $g(s;t)$ for R4-Unc-S60 at times $0hr$, $20hr$, and $1{,}116hr$. Because R4-Unc-S60 is uncorrelated, Theory-C and Theory-U yield identical results, thus only one is plotted in Fig.15. At $t=0$, all pores are saturated to $S^b=S_t^b$=60%, resulting in bubble states that form a vertical stripe in Fig.15. At $t>0$, the agreement between the snapshots of Theory-C/U and PNM is excellent, which validates the accuracy of both theories in uncorrelated networks.

Fig.16 shows the same plot as Fig.15 but for the correlated R4-Cor-S60 network. Since Theory-C and -U yield different predictions in this case, they are plotted separately. The snapshots of $g(s;t)$ correspond to the times $0hr$, $20hr$, and $200hr$ from the start of ripening. We see while Theory-C is in excellent agreement with the PNM, Theory-U is not. For this reason, we conclude that spatial correlations are indeed important to be taken into account via Theory-C and neglecting them via Theory-U can result in significant errors. Note that

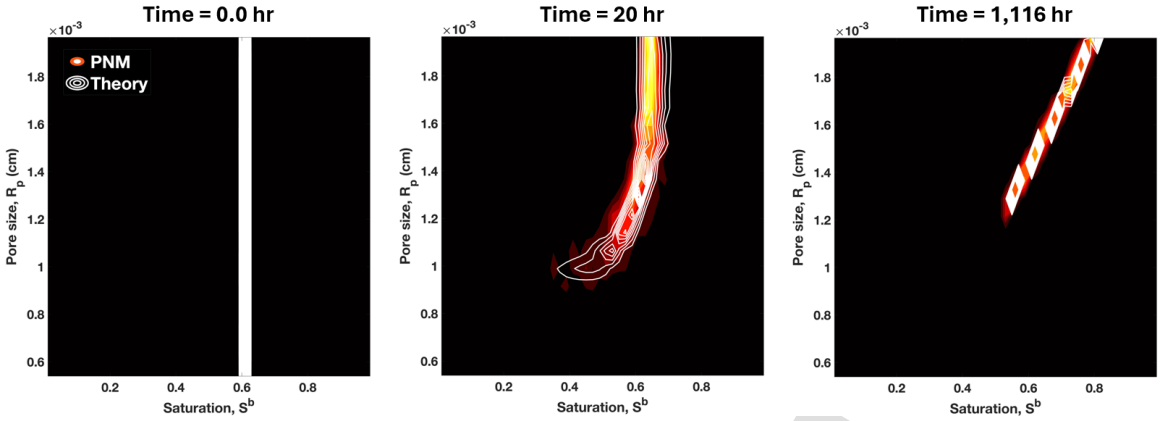

Figure 15: Snapshots of the distribution function $g(s;t)$ at three times (0, 20, and 1,116hr) in the phase space $s=(S^b, R_p)$ for the R4-Unc-S60 network in Table 1 computed via Theory-C/U and the PNM. Since the network is uncorrelated, Theory-C and -U yield identical results. The colored areas correspond to the PNM and the white contours to Theory-C/U. The heat maps for PNM use different shades of yellow, red, and black, in that order, to indicate decreasing values of $g(s;t)$.

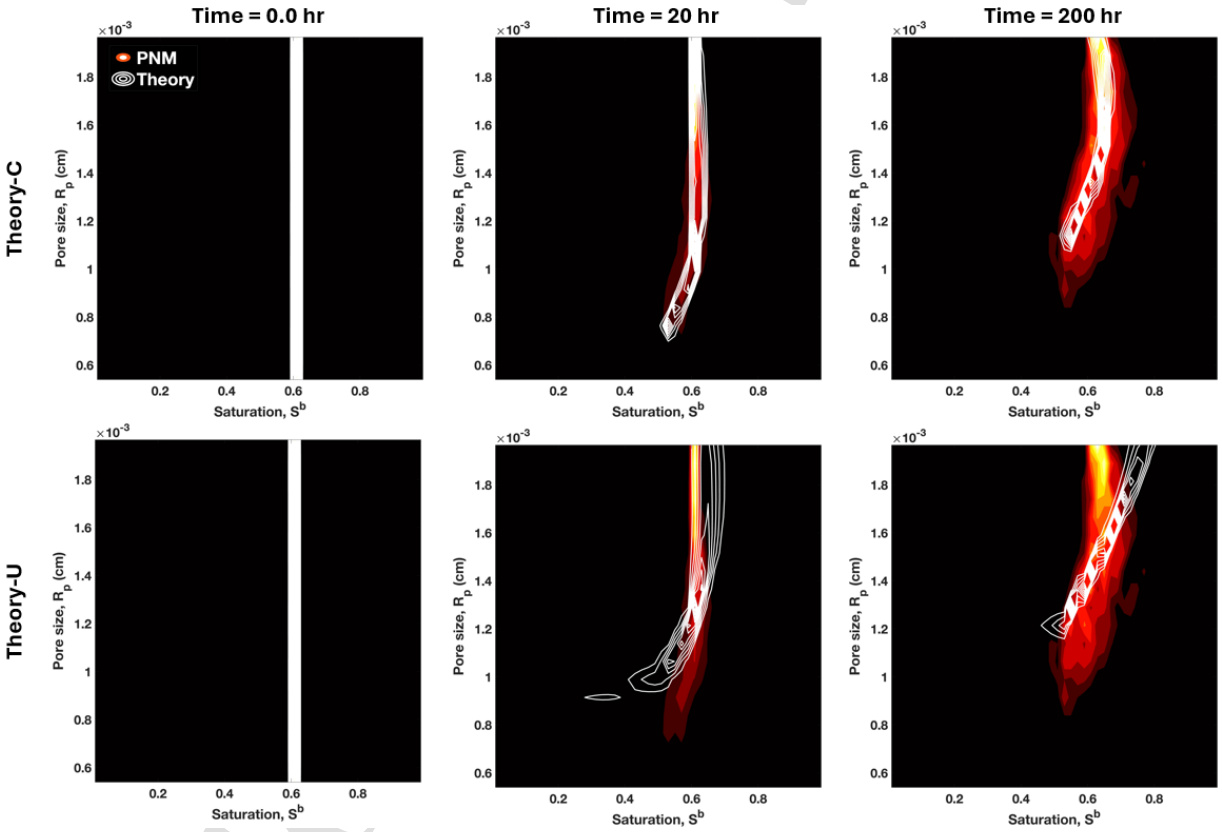

Figure 16: Snapshots of the distribution function $g(s;t)$ at three times (0, 20, and 200hr) in the phase space $s=(S^b, R_p)$ for the R4-Cor-S60 network in Table 1 computed via Theory-C/U and the PNM. Since the network is correlated, Theory-C (top row) and Theory-U (bottom row) are shown separately. The colored areas correspond to PNM and white contours to Theory-C/U. The heat maps for PNM use different shades of yellow, red, and black, in that order, to indicate decreasing values of $g(s;t)$.

in both Fig.15 and 16, small bubbles (i.e., in small R_p) dissolve and vanish due to their negative or leftward velocity (i.e., $dS^b/dt<0$) in the phase space. The late-time snapshots correspond to a near-equilibrium state in which all bubbles have similar curvature and Ostwald ripening ceases to evolve bubbles significantly.

6.5. Heterogeneous networks with complex initial bubble placements

Here, we increase the difficulty of our validation problem further by considering complex initial placements of bubbles inside correlated and uncorrelated networks. Specifically, we consider the Cmplx-Unc and Cmplx-Cor cases in Table 1 with $S_t^b=32\%$, which have networks identical to R4-Unc and R4-Cor from the last section except the initial bubble configurations are different. To initialize bubbles, we divide the pore sizes into three equal (in number) groups. In the first group (largest R_p), we randomly set local bubble saturations S^b between 5–35%. In the second (medium R_p), we set S^b between 35–65%, and in the third group (smallest R_p), we set S^b between 65–95%. Fig.17 shows the evolutions of the mean curvature $\bar{\kappa}$, mean bubble volume $\bar{V}^b$, and the fraction of survived bubbles F predicted by Theory-C and the PNM. Since Theory-U yields identical results for the correlated Cmplx-Cor and uncorrelated Cmplx-Unc, we only plot one of them. Fig.18 shows the corresponding evolution of $g(s;t)$ via three snapshots at times 0, 20, and 200hr and at equilibrium ($t\to\infty$). These PDFs are shown for Theory-C and the PNM, but not Theory-U because it yields results identical to Theory-C in the uncorrelated network and incurs significant errors in the correlated network. The snapshots at $t=0$ clearly illustrate how bubbles are initialized in phase space. Notice by placing low-S^b bubbles in larger pores (high R_p) we have increased their chance of survival at late times compared to Figs.15-16.

Once again, Theory-C is in good agreement with the PNM in Figs.17-18. We remark that unlike the theory of [14], Theory-C (and -U) accommodate complex initial conditions like those considered here, whereas [14] applies only to asymptotic regimes where any memory of the initial condition has been long forgotten.

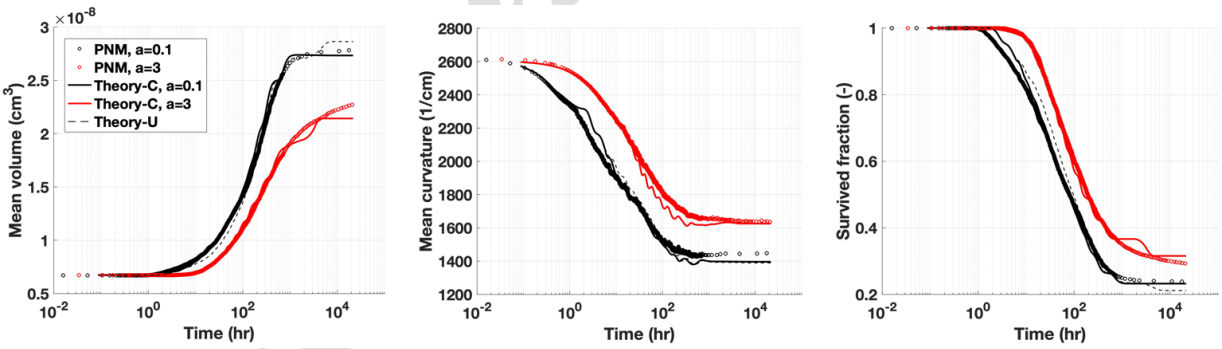

Figure 17: Comparison of (left) the mean bubble volume, (middle) mean bubble curvature, and (right) the fraction of survived bubbles versus time in the heterogeneous networks Cmplx-Unc and Cmplx-Cor in Table 1 computed via Theory-C, Theory-U, and the PNM. The networks are comprised of correlated (red) and uncorrelated (black) pore sizes drawn from a uniform distribution with $R_{het}=4$. Initial bubble saturation is $S_t^b=32\%$. Theory-U yields identical results for correlated and uncorrelated networks, thus only one curve is plotted.

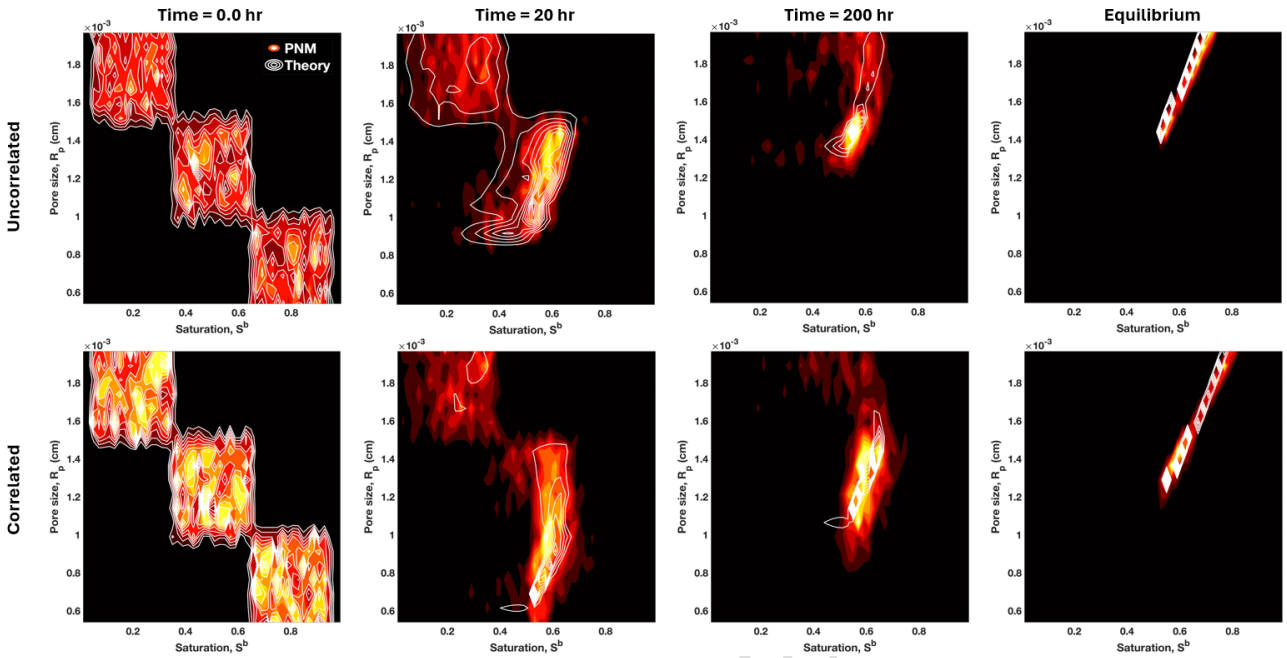

Figure 18: Snapshots of the distribution function $g(s;t)$ at three times (0, 20, and 200hr) and at equilibrium in the phase space $s=(S^b, R_p)$ for the Cmplx-Unc and Cmplx-Cor networks in Table 1 computed via Theory-C and the PNM. Theory-U is omitted because it yields results identical to Theory-C in the uncorrelated network (top row) and it deviates significantly in the correlated network (bottom row). The colored areas correspond to the PNM simulations and the white contours to Theory-C. The heat maps for PNM use different shades of yellow, red, and black, in that order, to indicate decreasing values of $g(s;t)$.

6.6. Heterogeneous networks with variable throat properties

In all cases considered thus far, the ratio A_t/L_t for all throats (cross-sectional area over length) was kept uniform to probe solely the impact of bubble states (S^b and R_p) on ripening dynamics. Here, we introduce another layer of complexity by allowing A_t/L_t to vary spatially. Specifically, we consider the vAL-Unc and vAL-Cor cases in Table 1, which are identical to Cmplx-Unc and Cmplx-Cor, respectively, except A_t/L_t is variable. Specifically, $R_{het}=4$, $S_t^b=32\%$, and the initial bubble placement is complex and the same as Section 6.5. While there are many ways to set A_t/L_t, we proceed as follows: If R_{p_1} and R_{p_2} denote the sizes of the two pores straddling a given throat, we compute the throat radius via $R_t=\min\{R_{p_1}, R_{p_2}\}/2$ then the throat area via $A_t=\pi R_t^2$. The throat length L_t is kept constant and equal to the lattice spacing. Thus, spatial variability in A_t/L_t is introduced through A_t alone. Fig.19 shows the evolutions of the mean curvature $\bar{\kappa}$, mean bubble volume $\bar{V^b}$, and the fraction of survived bubbles F versus time computed via Theory-C, Theory-U, and the PNM. Since Theory-U yields identical results for correlated and uncorrelated networks, only one is plotted.

As before, predictions from Theory-C are in good agreement with the PNM except at late times (to be discussed). By comparison, Theory-U performs satisfactorily in the uncorrelated vAL-Unc network, but poorly in the correlated vAL-Cor. Curiously, even in vAL-Unc, the prediction of F via Theory-U is off, which is likely because the parameter $(A/L)_s$ in Eq.20 is computed only once at $t=0$ and never updated again (unlike Theory-C). The corresponding plot of $g(s;t)$ versus time is similar to Fig.18 and thus omitted. Given

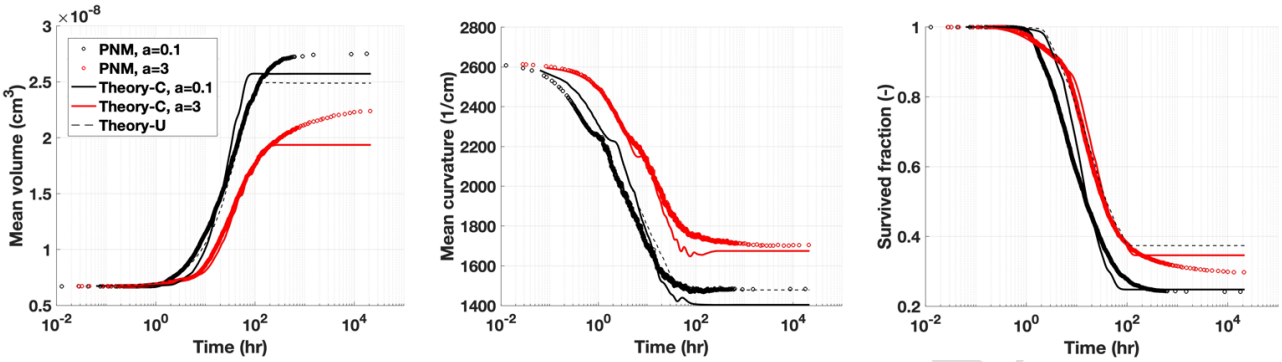

Figure 19: Comparison of (left) mean bubble volume, (middle) mean curvature, and (right) the fraction of survived bubbles versus time in the heterogeneous networks vAL-Unc and vAL-Cor computed via Theory-C, Theory-U, and the PNM. The networks are identical to those in Fig.17, except here throat dimensions (A_t/L_t) vary spatially. Pore sizes are drawn from a uniform distribution with $R_{het}=4$, and are either correlated (red) or uncorrelated (black). Initial bubble placement is complex (as Section 6.5) and S_t^b=32%. Theory-U yields identical results for correlated and uncorrelated networks, so only one is plotted.

the networks here constitute the most challenging of all in Table 1, we conclude that Theory-C is superior to Theory-U in predicting ripening kinetics, especially when applied to correlated networks.

7. Discussion

7.1. How to apply the bubble ripening theory

We have presented a theory to predict the Ostwald ripening kinetics of trapped bubbles in porous media. The theory describes the evolution of a distribution function, $g(s;t)$, of bubbles states, s, in time. Each bubble state consists of a pair of coordinates (S^b, R_p) in a statistical phase space over which $g(s;t)$ is defined. The saturation S^b denotes the fraction of the pore's volume the current bubble occupies, and R_p represents the size of the pore within which the bubble resides. The quantity $g(s;t)d\Omega$ with $d\Omega=dS^b dR_p$ is the number of bubbles in an infinitesimal patch of phase space centered at s. Our theory evolves $g(s;t)$ temporally using a population balance Eq.8, whose phase velocity $\boldsymbol{u}_s$ is determined by the mean-field approximation in Eq.14. But since Eq.14 is difficult to evaluate, due to the four-dimensional conditional probability $p(s'|s;t)$, two simplifications were introduced that led to Theory-C and -U. Their main difference is that Theory-U ignores spatial correlations while Theory-C preserves them. Section 6 demonstrated that Theory-C and -U generalize an existing theory by [14] for spherical bubbles in a homogeneous medium to deformed bubbles in a heterogeneous medium. Theory-C further extends to correlated microstructures, where Theory-U fails.

To apply Theory-C/U in practice, the starting point is often an X-ray μCT image of a porous material. A pore network can be extracted from such an image using one of many available algorithms, e.g., maximal ball [29], medial axis [30], and the watershed transform [31]. The network will yield a distribution of pore sizes (R_p) and throat sizes (A_t/L_t), which feed into the computations of $(A/L)_s$, κ_s^c, and κ^c via Eqs.17 and 21 used to estimate the phase velocity $\boldsymbol{u}_s$ (or dS_s^b/dt). An important assumption here, discussed further in Section 7.2, is that all pores are approximated to have the same *shape*, but not size. While we considered

semi-cubic pores throughout this work, whose local bubble curvatures obey Eq.7, other shapes are equally possible. In addition to pore-network statistics, the theory requires an initial condition. For Theory-U, no spatial information is needed and a mere knowledge of $g(s;0)$ is sufficient. The latter allows computing the initial number of bubbles n_b^0 via Eq.22 and the probability $p(R_p';0)$ that a pore of size R_p' is occupied by a bubble at $t=0$ via Eq.23. For Theory-C, we need some spatial information to be able to compute the conditional probability $p(R_p'|R_p;0)$, which quantifies the likelihood that a bubble within a pore of size R_p is connected to another within a pore of size R_p' at $t=0$. Such information may be captured by the same X-ray μCT image used to scan the specimen and visualize trapped bubbles, or simulated using a numerical model (e.g., PNM, lattice Boltzmann). Specifically, we need $n^0_{R_p'R_p}$ that quantifies the number of throats connecting bubble-occupied pores with sizes R_p and R_p' at $t=0$. Inserting this quantity into Eq.B.3 yields $p(R_p'|R_p;0)$. Once parameterized, Theory-C and -U can predict ripening dynamics orders of magnitude faster than PNM because their costs do not scale with the porous sample's size or the number of bubbles tracked.

The evolution of $g(s;t)$ so predicted informs which pores are occupied by bubbles, and to what saturation, at time t. When coupled to upscaled models of a porous medium, such bubble-occupancy statistics can inform how the macroscopic properties of the sample, like relative permeability [32], evolve over time. The implications of such predictive understanding would allow, e.g., estimating degradations or enhancements of fluid injection/withdrawal in underground hydrogen storage as well as water management in fuel cells.

7.2. Limitations of the proposed theory

As discussed above, Theory-U is limited to porous media devoid of any spatial correlation. While Theory-C removes this limitation and allows predicting the evolution of bubble statistics within correlated microstructures, it has one glaring limitation: *it does not account for interactions between bubbles that are separated by more than one throat*. Concretely, if a group of bubbles occupy pores of size R_p and another group occupies pores of size R_p', the two *cannot* exchange mass via ripening *if* $p(R_p'|R_p;0)=0$. This can occur if the network is correlated and the initial placement of bubbles in the porous medium is very sparse and non-random (i.e., certain pore sizes are occupied but not others). Recall, $p(R_p'|R_p;0)$ represents the probability of communication between a bubble and its adjacent, or *first-order*, neighbor but does not capture the communication with farther, or higher-order, neighbors. Under these conditions, bubbles in pore sizes R_p and R_p' evolve independently from each other. Fig.20 shows a contrived counterexample that amplifies this shortcoming.

At $t=0$, sub-critical bubbles are placed in the largest 20% of pore sizes (S_s^b assigned randomly between 5–35%) and super-critical bubbles in the smallest 20% of pore sizes (S_s^b assigned randomly between 65–95%). The top row of Fig.20 corresponds to a spatially uncorrelated network (R4-Unc in Table 1), while the bottom row to a correlated pore network (R4-Cor in Table 1). In the uncorrelated network, the agreement between Theory-C and the PNM is good. However, in the correlated network, bubbles in large and small pore sizes are fully disconnected (i.e., there is more than one throat between them). Hence, $p(R_p'|R_p;0)=0$ holds for bubbles occupying pore sizes R_p and R_p'. By Eq.18, this implies $p(R_p'|R_p;t)=0$ for all $t>0$. Physically, this means the two bubble groups evolve and equilibrate independently from each other as can be seen in Fig.20.

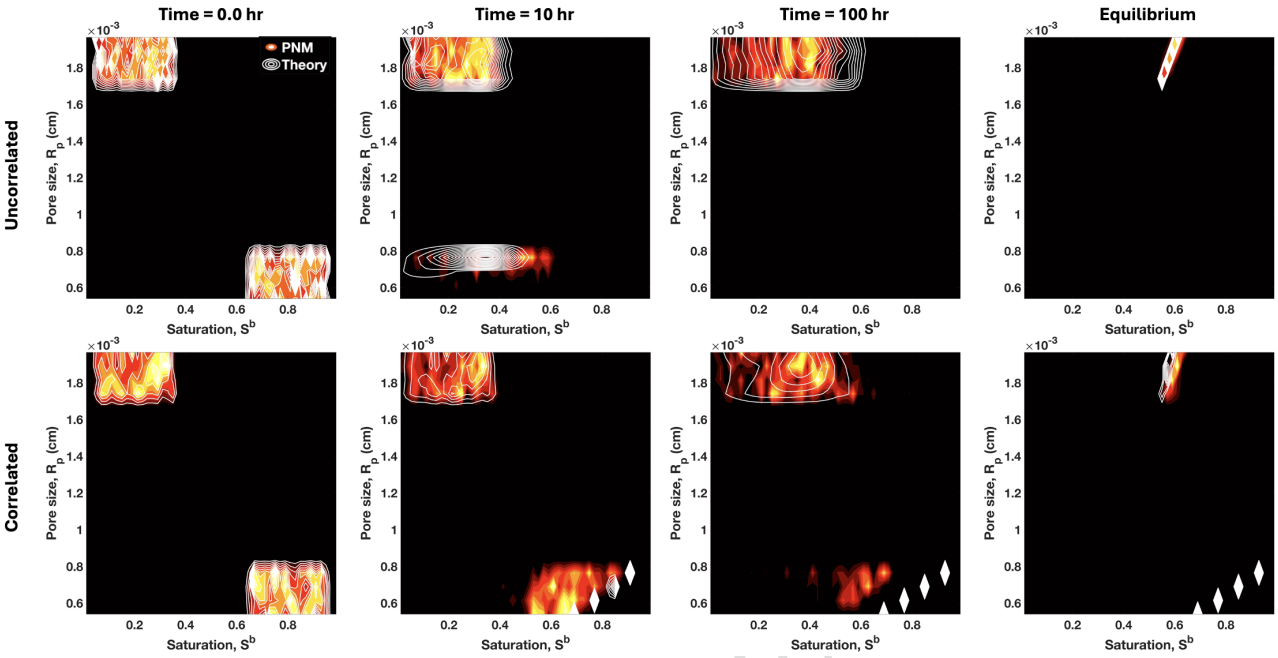

Figure 20: Counterexample highlighting the limitation of Theory-C in capturing bubble interactions between higher-order neighbors (i.e., more than one throat apart). Snapshots of the distribution function $g(s;t)$ at three times (0, 10, and $100hr$) and at equilibrium in the phase space $s=(S^b, R_p)$ for uncorrelated (top row) and correlated (bottom row) networks with $R_{het}=4$ computed via Theory-C and the PNM. Theory-U is omitted because it yields results identical to Theory-C in the uncorrelated network (top row) for both networks. The colored areas correspond to PNM simulations and the white contours to Theory-C. The heat maps for PNM use different shades of yellow, red, and black, in that order, to indicate decreasing values of $g(s;t)$.

By contrast, Theory-U yields the same prediction for both correlated and uncorrelated networks, which is identical to that of Theory-C in the uncorrelated network (top row of Fig.20). In this sense, Theory-U is more robust because even when it is wrong, its failure is not unphysical. The reason lies in the fact that each bubble in Theory-U interacts with the same mean field that is, in turn, informed by *all* the bubbles. Put differently, every bubble pair in Theory-U has some non-zero communication, unlike Theory-C. We suspect this shortcoming of Theory-C is the main reason for the larger late-time errors observed in Section 6 (e.g., top-middle plot of Fig.14). To rectify Theory-C, interactions between higher-order neighboring bubbles must be captured, which can be done by augmenting $p(R_p'|R_p;t)$ to include the connectivity between bubbles multiple throats apart. The specifics are subject to ongoing research and outside the scope of this paper.

A second limitation, alluded to in Section 7.1, is that all pores are assumed to have the same *shape*. This is clearly not the case for a network extracted from an X-ray μCT image of a porous material. Each shape is associated with a constitutive relation different from Eq.7, describing the dependence of a trapped bubble's curvature κ_i on its volume V_i^b. Currently, in Theory-C/U, an average pore shape must be assumed so the same constitutive relation (Eq.7 or equivalent) can be applied to all pores. If pore-shape heterogeneity were to be captured explicitly, the bubble state s must include, aside from pore size and bubble saturation, *pore shape* as an independent coordinate. This renders the phase space 3D, as opposed to 2D in its current form.

A third limitation is that the wetting phase is assumed to be hydrodynamically immobile with uniform pressure. While this is an acceptable approximation to subsurface conditions where trapped bubbles interact far away from wells or during extended shut-in periods, months in hydrogen storage and years to centuries in CO_2 sequestration, it is a poor assumption otherwise. Background flow of the wetting phase introduces another mechanism for dissolved species to be transported between bubbles, which renders ripening not just dependent on gradients in interfacial curvature but also on advection. Extending the PNM to account for such advective mass transfer is straightforward [33], but generalizing Theory-C/U is more difficult.

The fourth and final limitation of Theory-C/U is that bubbles occupy only one pore each, which does not change over time during ripening. This is reflected by our approximation in Section 4.2 that the phase velocity is $\boldsymbol{u}_s \approx (dS^b/dt, 0)$ with no vertical component (i.e., $dR_p/dt = 0$). The fact that bubbles occupy only one pore also allowed us to use pore size, R_p, as one of the components of a bubble's state, which would otherwise be ill-defined. Previous work [8] showed even single-pore occupying bubbles can hydrodynamically displace from one pore to another during growth by ripening. Such displacements, called *bubble dislocation*, result in $dR_p/dt \neq 0$ in phase space. From past experience, we suspect the frequency of dislocation-induced changes in bubble states to be negligible compared to ripening-induced changes, i.e., $dS^b/dt \gg dR_p/dt$.

7.3. Limitations of the validation process

Aside from inherent limitations of Theory-C/U in their present form outlined in Section 7.2, there are shortcomings to our validation process itself. These include the assumptions that bubbles are incompressible, have zero contact angle (i.e., perfectly non-wetting), pores have a semi-cubic shape that obey Eq.7, and the pore networks are topologically 2D (though geometrically 3D) with a fixed coordination number. We expect none of these to impair the predictive accuracy of Theory-C/U, but future work is needed to substantiate such extended ranges of applicability. Our rationale is based on the fact that pore shape and bubble contact angle alter only the specific form and regularity (i.e., continuity) of the κ_i–V_i^b relation in Eq.7 [11], and the governing equations for compressible bubbles (e.g., air, H_2, CO_2) assume a similar form as Section 4.3 [2]. Now, if non-zero contact angles cause the emergence of disconnected pockets of wetting phase with different pressures [21], then this would pose challenges intrinsic to our theory and not just the validation process.

7.4. Implications for continuum-scale modeling

Continuum (or upscaled) representations of Ostwald ripening solve a saturation equation of the form:

$$\frac{\partial S_t^b}{\partial t} = \frac{\partial}{\partial x}\left(K \frac{\partial S_t^b}{\partial x}\right) \tag{25}$$

where $K \sim dP_c/dS_t^b$ [24, 27] and P_c is the macroscopic capillary pressure of bubbles in the porous medium. Solving Eq.25, by decomposing the porous domain into grid blocks and discretizing Eq.25, yields estimates of ripening kinetics and the evolution of the upscaled saturation S_t^b at the *macroscale*. However, Eq.25 is only valid if *all* bubbles inside each grid block are in thermodynamic equilibrium (i.e., have identical interfacial curvature) at all time. This assumption is embedded in the existence of a static (in time) relationship between

P_c and S_t^b. The kinetic theory formulated in this work pertains to the *pore scale*, and would yield estimates of exactly *when* such equilibration would take place within each macroscale grid block. If this time-to-equilibrium is larger than the timescale over which grid blocks exchange mass via ripening, Eq.25 is no longer valid and a continuum PDE that captures some sort of temporal "memory" (e.g., convolution integrals) becomes necessary. We note the final equilibrium state of bubbles (thus P_c and S_t^b) can be computed via a theory proposed by [11], or by calculating the asymptotic value of $g(s;t)$ in Theory-C/U herein as $t \to \infty$.

8. Conclusion

We presented a theory that predicts the evolution kinetics in the statistics of a population of trapped bubbles inside a porous medium with arbitrary heterogeneity and spatial correlation in pore/throat sizes due to Ostwald ripening. The theory consists of a population balance equation in terms of the distribution function $g(s;t)$ of bubble states s, and a mean-field (or closure) approximation for the phase velocity $\boldsymbol{u}_s$. The variables s, $g(s;t)$, and $\boldsymbol{u}_s$ are all defined on a 2D phase space that consists of two coordinates: (1) R_p, or the pore size occupied by each bubble; and (2) S^b, or the bubble saturation (i.e., volume fraction) occupying the pore. The formulation of $\boldsymbol{u}_s$ led to two variants of our theory: (1) Theory-C, where spatial correlations are honored; an (2) Theory-U, where such correlations are neglected. We systematically validated Theory-C/U against pore-network (PNM) simulations of ripening in a range of homogeneous, heterogeneous, correlated, and uncorrelated microstructures that are initially occupied by bubbles with different saturations and spatial placements. In all cases, Theory-C was in good agreement with the PNM exhibiting superior predictive accuracy over Theory-U without any parameter calibration. By contrast, Theory-U was accurate only when applied to uncorrelated media. A key result was the comparison of Theory-C/U against an existing theory by [14] for homogeneous networks occupied by spherical bubbles, and the demonstration that Theory-C/U successfully generalizes the latter to heterogeneous networks and non-spherical (deformed) bubbles.

Despite its advantages, we highlighted and discussed key shortcomings of Theory-C. Chief among them were the inability to account for mass exchange between remote bubbles in a *correlated* network (separated by more than one throat), the constraint that bubbles span no more than one pore, and for them to remain hydrodynamically immobile during ripening. On the first limitation, an extreme (thus unlikely in practice) counterexample was devised to demonstrate how Theory-C may fail in an unphysical way, while Theory-U yields an inaccurate but physical result. The latter speaks to the robustness of Theory-U over Theory-C. Future research should aim at removing these limitations. Theory-C/U allow estimating the timescale of ripening, quantifying which pores are occupied by bubbles and up to what fraction at any given time, and the latter's impact on storage and hydraulic properties of porous media. The implications extend to applications like underground H_2 storage, geologic CO_2 sequestration, and optimal design of fuel cells and electrolyzers.

Acknowledgments

This material is based upon work supported by the National Science Foundation under Grant No. CBET-2348723. N.B. and L.A. gratefully acknowledge funding support from the William A. Fustos Family Professorship in Energy and Mineral Engineering at the Pennsylvania State University. We acknowledge the Institute for Computational and Data Sciences (ICDS) at Penn State University for computational resources.

Declaration of interests

The authors declare that they have no known competing financial interests or personal relationships that could have appeared to influence the work reported in this paper.

Appendix A. Derivation of κ_s^c and $(A/L)_s$ in Theory-C

We derive the expressions in Eq.17 below. If we substitute Eqs.15 and 16 into Eq.14b and expand the integral $\int_{s'} d\Omega = \int_{R'_p} \int_{S'^b} dS'^b dR'_p$, we can perform the following series of straightforward manipulations:

$$\begin{aligned}
\kappa_s^c &= \left(\frac{A}{L}\right)_s^{-1} \int_{s'} p(s'|s) \frac{A_{ss'}}{L_{ss'}} \kappa_{s'}\, d\Omega \\
&\approx \left(\frac{A}{L}\right)_s^{-1} \int_{R'_p} \int_{S'^b} p(R'_p|R_p)\, p(S'^b|R'_p) \frac{A_{R_p R'_p}}{L_{R_p R'_p}} \kappa_{s'}\, dS'^b dR'_p \\
&= \left(\frac{A}{L}\right)_s^{-1} \int_{R'_p} p(R'_p|R_p) \frac{A_{R_p R'_p}}{L_{R_p R'_p}} \Big(\underbrace{\int_{S'^b} p(S'^b|R'_p)\, \kappa_{s'} dS'^b}_{:=\bar{\kappa}_{R'_p}} \Big) dR'_p = \left(\frac{A}{L}\right)_s^{-1} \int_{R'_p} p(R'_p|R_p) \frac{A_{R_p R'_p}}{L_{R_p R'_p}} \bar{\kappa}_{R'_p} dR'_p
\end{aligned} \tag{A.1}$$

which proves the κ_s^c expression in Eq.17b. Similarly for $(A/L)_s$, we can write the following:

$$\begin{aligned}
\left(\frac{A}{L}\right)_s &= \int_{s'} p(s'|s) \frac{A_{ss'}}{L_{ss'}}\, d\Omega \\
&\approx \int_{R'_p} \int_{S'^b} p(R'_p|R_p)\, p(S'^b|R'_p) \frac{A_{R_p R'_p}}{L_{R_p R'_p}}\, dS'^b dR'_p \\
&= \int_{R'_p} p(R'_p|R_p) \frac{A_{R_p R'_p}}{L_{R_p R'_p}} \Big(\underbrace{\int_{S'^b} p(S'^b|R'_p) dS'^b}_{=1} \Big) dR'_p = \int_{R'_p} p(R'_p|R_p) \frac{A_{R_p R'_p}}{L_{R_p R'_p}} dR'_p
\end{aligned} \tag{A.2}$$

which proves the second expression in Eq.17b.

Appendix B. Derivation of $p(R'_p|R_p;t)$ in Theory-C

To derive Eq.18, we begin with a few definitions with reference to Fig.B.1. Consider two pore types with sizes R_p and R'_p in a pore network. The ovals in Fig.B.1 represent the total number of *bubble-occupied* pores in each category at $t=0$, denoted by $n^0_{R_p}$ and $n^0_{R'_p}$. The total number of surviving bubbles in each pore type at later times can be computed from the distribution function $g(s;t)$ as follows:

$$n_{R_p} = g(R_p;t)\, dR_p = \int_{S^b} g(S^b, R_p;t) dS^b\, dR_p\,, \quad n_{R'_p} = g(R'_p;t)\, dR'_p = \int_{S'^b} g(S'^b, R'_p;t) dS'^b\, dR'_p \tag{B.1}$$

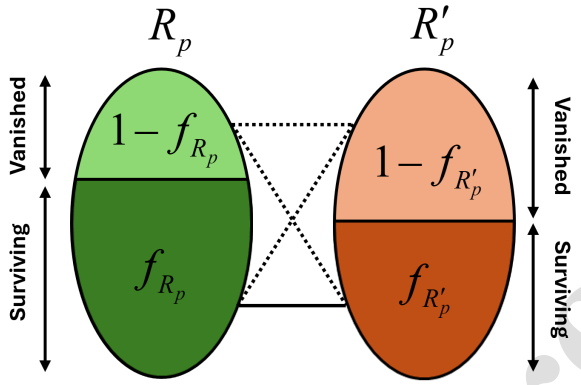

Figure B.1: Two pore types with sizes R_p (green) and R'_p (red) in a pore network. Each oval represents the total number of *bubble-occupied* pores in each category at $t=0$. At later times, a fraction of $1-f_{R_p}$ and $1-f_{R'_p}$ from each category dissolves and vanishes due to ripening. The lines denote throats linking the vanished and surviving bubbles in each pore type to each other. Dashed throats are lost connections during this dissolution process, and are the ones subtracted from $n_{R_pR'_p}$ in Eq.B.5.

Hence, the fraction of *initial* bubbles that have survived in each pore type at any given time is:

$$f_{R_p} = \frac{n_{R_p}}{n^0_{R_p}}, \qquad f_{R'_p} = \frac{n_{R'_p}}{n^0_{R'_p}} \tag{B.2}$$

as depicted in Fig.B.1. The rest of the bubbles (fractions $1-f_{R_p}$ and $1-f_{R'_p}$) have dissolved and vanished due to ripening. Let $z^b_{R_p}$ and $z^b_{R'_p}$ be the *average* coordination number of each pore type, which only counts neighbors that are occupied by a bubble (i.e., not a property of the network, and a time-dependent quantity). We denote their initial values at $t=0$ by $z^b_{R_p,0}$ and $z^b_{R'_p,0}$. Finally, let $n_{R_pR'_p}$ represent the number of throats that emanate from bubbles residing in pores with size R_p and terminate at bubbles residing in pores with size R'_p. Notice $n_{R_pR'_p}=n_{R'_pR_p}$ must hold, as it is a symmetric quantity. Let $n^0_{R_pR'_p}$ be the value at $t=0$.

With these definitions in place, we can formulate $p(R'_p|R_p;t)$ as follows:

$$p(R'_p|R_p;t)\,dR'_p = \frac{n_{R'_pR_p}}{\sum_{R'_p} n_{R'_pR_p}} = \frac{n_{R'_pR_p}}{n_{R_p} z^b_{R_p}} \tag{B.3}$$

where the denominator is the total number of throats that emanate from pore type R_p into bubble-occupied pores of *any* type. Note that given the symmetry of $n_{R_pR'_p}$, the following identity must hold:

$$n_{R_p} z^b_{R_p}\, p(R'_p|R_p;t)\,dR'_p = n_{R'_p} z^b_{R'_p}\, p(R_p|R'_p;t)\,dR_p \tag{B.4}$$

To evaluate Eq.B.3, we need an expression for $n_{R_pR'_p}$. Fig.B.1 shows that if $1-f_{R_p}$ and $1-f_{R'_p}$ fractions of bubbles in each pore type vanish, then the throats depicted by the dashed lines are lost, which link bubbles from f_{R_p} to $1-f_{R'_p}$, $1-f_{R_p}$ to $f_{R'_p}$, and $1-f_{R_p}$ to $1-f_{R'_p}$. Subtracting the lost throats from $n^0_{R_pR'_p}$ yields:

$$\begin{aligned} n_{R'_p,R_p} = n^0_{R'_p,R_p} &- f_{R_p}\, n^0_{R_p}\, z^b_{R_p,0}\, p(R'_p|R_p;0)\,dR'_p\,(1-f_{R'_p}) \\ &- (1-f_{R_p})\, n^0_{R_p}\, z^b_{R_p,0}\, p(R'_p|R_p;0)\,dR'_p\, f_{R'_p} \\ &- (1-f_{R_p})\, n^0_{R_p}\, z^b_{R_p,0}\, p(R'_p|R_p;0)\,dR'_p\,(1-f_{R'_p}) \end{aligned} \tag{B.5}$$

Notice $n_{R_p} = f_{R_p} n^0_{R_p}$ and $(1 - f_{R_p})\, n^0_{R_p}$ are the number of surviving and vanished bubbles in pore type R_p, respectively. Multiplying them by $z^b_{R_p,0}\, p(R'_p|R_p;0)\, dR'_p$ yields the number of throats emanating from such bubbles and terminating at the *initially* bubble-occupied pores with size R'_p. A final multiplication by $f_{R'_p}$ or $1 - f_{R'_p}$ yields the number of throats that correspond to the dashed lines in Fig.B.1.

Eq.B.5 can be simplified by writing Eq.B.3 at $t=0$ as:

$$n^0_{R'_p R_p} = n^0_{R_p}\, z^b_{R_p,0}\, p(R'_p|R_p;0)\, dR'_p \tag{B.6}$$

and substituting it into Eq.B.5, followed by some algebraic manipulation, to obtain:

$$n_{R'_p,R_p} = f_{R_p}\, f_{R'_p}\, n^0_{R'_p,R_p} \tag{B.7}$$

Summing this expression over all R'_p yields:

$$\sum_{R'_p} n_{R'_p R_p} = f_{R_p} \sum_{R'_p} f_{R'_p}\, n^0_{R'_p R_p} = f_{R_p}\, n^0_{R_p}\, z^b_{R_p,0} \int_{R'_p} f_{R'_p}\, p(R'_p|R_p;0)\, dR'_p \tag{B.8}$$

where in the second equality, we have used Eq.B.6. Substituting Eqs.B.7 and B.8 into Eq.B.3, and making use of Eq.B.6 once again, we obtain the final expression for $p(R_p|R'_p;t)$ given by:

$$p(R'_p|R_p;t) = \frac{f_{R'_p}\, p(R'_p|R_p;0)}{\int_{R'_p} f_{R'_p}\, p(R'_p|R_p;0)\, dR'_p} \tag{B.9}$$

which is the same as Eq.18. While not used explicitly anywhere in Theory-C, we may estimate the bubble-occupied coordination number $z^b_{R_p}$ at any given time as follows:

$$z^b_{R_p} = \frac{\sum_{R'_p} n_{R'_p R_p}}{n_{R_p}} = \frac{f_{R_p} n^0_{R_p} z^b_{R_p,0} \int_{R'_p} f_{R'_p}\, p(R'_p|R_p;0)\, dR'_p}{f_{R_p}\, n^0_{R_p}} = z^b_{R_p,0} \int_{R'_p} f_{R'_p}\, p(R'_p|R_p;0)\, dR'_p \tag{B.10}$$

Appendix C. Derivation of $p(R'_p;t)$ in Theory-U

To derive Eq.22, we first establish the following relation for $p(R'_p;0)$:

$$p(R'_p;0) = \frac{\int_{S'^b} g(S'^b, R'_p;0)\, dS'^b}{\int_{R'_p} \int_{S'^b} g(S'^b, R'_p;0)\, dS'^b\, dR'_p} = \frac{g(R'_p;0)}{n^0_b} \tag{C.1}$$

where n^0_b is the total number of bubbles in the pore network at $t=0$. Moreover, recall:

$$f_{R'_p} = \frac{n_{R'_p}}{n^0_{R'_p}} = \frac{g(R'_p;t)}{g(R'_p;0)} \tag{C.2}$$

follows from the definitions in Eqs.B.1 and B.2.

Using Eq.C.1, Eq.C.2, and $p(R'_p|R_p;t) \approx p(R'_p;t)$ from Eq.19, we can approximate:

$$\begin{aligned} \int_{R'_p} f_{R'_p}\, p(R'_p|R_p;0)\, dR'_p &\approx \int_{R'_p} f_{R'_p}\, p(R'_p;0)\, dR'_p \\ &= \int_{R'_p} \frac{g(R'_p;t)}{g(R'_p;0)}\, p(R'_p;0)\, dR'_p = \frac{1}{n^0_b} \int_{R'_p} g(R'_p;t)\, dR'_p = \frac{n_b}{n^0_b} = F \end{aligned} \tag{C.3}$$

for the denominator of Eq.B.9. In the last three equalities, we have used the definitions of n_b, n_b^0, and F introduced in Eq.22. Using $p(R_p'|R_p;t) \approx p(R_p';t)$ again for the numerator of Eq.B.9, we get:

$$p(R_p';t) = \frac{f_{R_p'}\, p(R_p';0)}{F} \tag{C.4}$$

which is the same as Eq.22. This concludes our derivation.

Appendix D. PDFs of bubble saturation in patterned networks

Fig.D.2 depicts the PDFs of the local bubble saturations in pores corresponding to the results in Fig.12. These PDFs represent the marginal distribution $g(S^b;t)/n_b$; where bubbles in both pore sizes are combined into a single distribution function. At $t=0$, the PDFs are Dirac deltas centered at S^b =60% as shown by the vertical green lines in Fig.D.2. At early and late times, the PDFs obtained from Theory-C capture the trends observed from the PNM in *all* networks, whereas Theory-U captures the trend in the least correlated network Pt-16. Specifically, Theory-C reproduces a short peak observed at early times in all networks, which progressively moves to the left as smaller bubbles vanish. This peak is also seen in the PNM, but its location occurs either earlier or later than that predicted by Theory-C. Given the networks are *ordered*, small errors in the theories tend to amplify over time, rendering the interpretation of the results in Fig.D.2 difficult. Notice once again, predictions from Theory-C asymptote to those of Theory-U in going from Pt-4 to Pt-16.

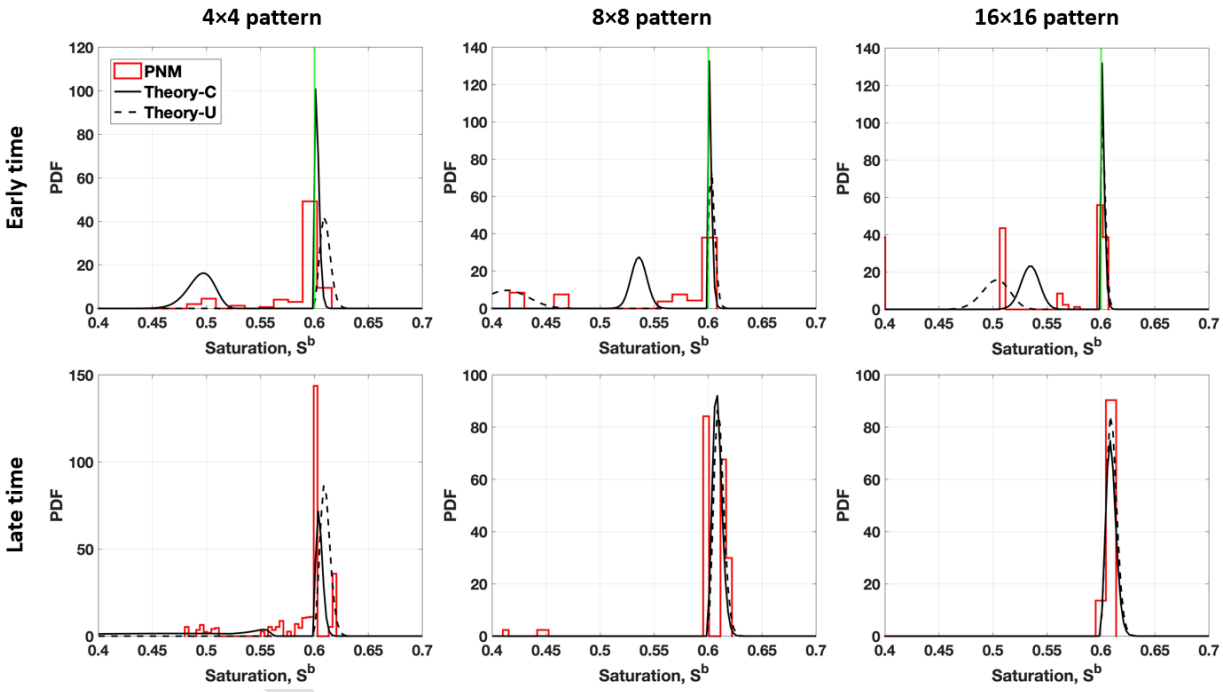

Figure D.2: Comparison of PDFs of local bubble saturation in pores predicted by the PNM, Theory-C, and Theory-U at early and late times for the Pt-4 (4×4 pattern), Pt-8 (8×8 pattern), and Pt-16 (16×16 pattern) networks in Table 1. The early- and late-time snapshots correspond to $4hr$ and $10hr$ in Pt-4, $1hr$ and $10hr$ in Pt-8, and $0.5hr$ and $4hr$ in Pt-16 from the start of ripening. The vertical green lines in the top row represent the initial conditions, which are Dirac deltas centered at S^b =60%.

References

[1] W. Ostwald, Studien über die bildung und umwandlung fester körper, Zeitschrift für physikalische Chemie 22 (1) (1897) 289–330.

[2] N. Bueno, L. Ayala, Y. Mehmani, Ostwald ripening of multi-component bubbles in porous media: A theory and a pore-scale model of how bubble populations equilibrate, Advances in Water Resources 182 (2023). doi:10.1016/j.advwatres.2023.104581.

[3] S. Bachu, Co2 storage in geological media: Role, means, status and barriers to deployment, Progress in energy and combustion science 34 (2) (2008) 254–273.

[4] M. Andersson, S. Beale, M. Espinoza, Z. Wu, W. Lehnert, A review of cell-scale multiphase flow modeling, including water management, in polymer electrolyte fuel cells, Applied Energy 180 (2016) 757–778.

[5] J. K. Lee, C. Lee, K. F. Fahy, P. J. Kim, K. Krause, J. M. LaManna, E. Baltic, D. L. Jacobson, D. S. Hussey, A. Bazylak, Accelerating bubble detachment in porous transport layers with patterned through-pores, ACS Applied Energy Materials 3 (10) (2020) 9676–9684.

[6] A. J. Bray, Theory of phase-ordering kinetics, Advances in Physics 51 (2) (2002) 481–587.

[7] C. Wang, Y. Mehmani, K. Xu, Capillary equilibrium of bubbles in porous media, Proceedings of the National Academy of Sciences 118 (17) (2021) e2024069118.

[8] Y. Mehmani, K. Xu, Capillary equilibration of trapped ganglia in porous media: A pore-network modeling approach, Advances in Water Resources 166 (8 2022). doi:10.1016/j.advwatres.2022.104223.

[9] K. Xu, R. Bonnecaze, M. Balhoff, Egalitarianism among bubbles in porous media: an ostwald ripening derived anticoarsening phenomenon, Physical review letters 119 (26) (2017) 264502.

[10] J. A. de Chalendar, C. Garing, S. M. Benson, Pore-scale modelling of ostwald ripening, Journal of Fluid Mechanics 835 (2018) 363–392.

[11] Y. Mehmani, K. Xu, Pore-network modeling of ostwald ripening in porous media: How do trapped bubbles equilibrate?, Journal of Computational Physics 457 (5 2022). doi:10.1016/j.jcp.2022.111041.

[12] I. M. Lifshitz, V. V. Slyozov, The kinetics of precipitation from supersaturated solid solutions, Journal of physics and chemistry of solids 19 (1-2) (1961) 35–50.

[13] C. Wanger, Theorie der alterung von niederschlagen durch umlosen, Z. Elektrochem. 65 (1961) 581–591.

[14] Y. Yu, C. Wang, J. Liu, S. Mao, Y. Mehmani, K. Xu, Bubble coarsening kinetics in porous media, Geophysical Research Letters 50 (1) (2023) e2022GL100757.

[15] C. Garing, J. A. de Chalendar, M. Voltolini, J. B. Ajo-Franklin, S. M. Benson, Pore-scale capillary pressure analysis using multi-scale x-ray micromotography, Advances in Water Resources 104 (2017) 223–241.

[16] N. Joewondo, V. Garbin, R. Pini, Experimental evidence of the effect of solute concentration on the collective evolution of bubbles in a regular pore-network, Chemical Engineering Research and Design 192 (2023) 82–90.

[17] S. Goodarzi, Y. Zhang, S. Foroughi, B. Bijeljic, M. J. Blunt, Trapping, hysteresis and ostwald ripening in hydrogen storage: A pore-scale imaging study, International Journal of Hydrogen Energy 56 (2024) 1139–1151.

[18] N. Joewondo, V. Garbin, R. Pini, Nonuniform collective dissolution of bubbles in regular pore networks, Transport in Porous Media 141 (3) (2022) 649–666.

[19] D. Singh, H. A. Friis, E. Jettestuen, J. O. Helland, A level set approach to ostwald ripening of trapped gas bubbles in porous media, Transport in Porous Media 145 (2) (2022) 441–474.

[20] D. Singh, H. A. Friis, E. Jettestuen, J. O. Helland, Pore-scale ostwald ripening of gas bubbles in the presence of oil and water in porous media, Journal of Colloid and Interface Science 647 (2023) 331–343.

[21] D. Singh, H. A. Friis, E. Jettestuen, J. O. Helland, Ripening of capillary-trapped co2 ganglia surrounded by oil and water at the pore scale: Impact of reservoir pressure and wettability, Energy & Fuels 38 (10) (2024) 8853–8874.

[22] Y. Mehmani, T. Anderson, Y. Wang, S. Aryana, I. Battiato, H. Tchelepi, A. Kovscek, Striving to translate shale physics across ten orders of magnitude: What have we learned?, Earth-Science Reviews 223 (2021). doi:10.1016/j.earscirev.2021.103848.

[23] K. Xu, Y. Mehmani, L. Shang, Q. Xiong, Gravity-induced bubble ripening in porous media and its impact on capillary trapping stability, Geophysical Research Letters 46 (23) (2019) 13804–13813.

[24] Y. Li, C. Garing, S. M. Benson, A continuum-scale representation of ostwald ripening in heterogeneous porous media, Journal of Fluid Mechanics 889 (2020) A14.

[25] Y. Li, F. M. Orr Jr, S. M. Benson, Long-term redistribution of residual gas due to non-convective transport in the aqueous phase, Transport in Porous Media 141 (1) (2022) 231–253.

[26] M. J. Blunt, Ostwald ripening and gravitational equilibrium: Implications for long-term subsurface gas storage, Physical Review E 106 (4) (2022) 045103.

[27] Y. Mehmani, K. Xu, A continuum theory of diffusive bubble depletion in porous media, Advances in Water Resources 185 (2024) 104625.

[28] A. G. Hanson, B. Kutchko, G. Lackey, D. Gulliver, B. R. Strazisar, K. A. Tinker, F. Haeri, R. Wright, N. Huerta, S. Baek, et al., Subsurface hydrogen and natural gas storage: State of knowledge and research recommendations report (2022).

[29] D. Silin, T. Patzek, Pore space morphology analysis using maximal inscribed spheres, Physica A: Statistical mechanics and its applications 371 (2) (2006) 336–360.

[30] W. B. Lindquist, S.-M. Lee, D. A. Coker, K. W. Jones, P. Spanne, Medial axis analysis of void structure in three-dimensional tomographic images of porous media, Journal of Geophysical Research: Solid Earth 101 (B4) (1996) 8297–8310.

[31] S. Beucher, C. Lantuéjoul, Use of watersheds in contour detection, in: International Workshop on Image Processing: Real-time Edge and Motion Detection/Estimation, Rennes, France, 1979.

[32] J. Bear, Dynamics of fluids in porous media, Courier Corporation, 2013.

[33] Y. Mehmani, M. T. Balhoff, Mesoscale and hybrid models of fluid flow and solute transport, Reviews in Mineralogy and Geochemistry 80 (2015) 433–459. doi:10.2138/RMG.2015.80.13.
URL http://dx.doi.org/10.2138/rmg.2015.80.13

- Theory for predicting Ostwald ripening kinetics of bubbles in porous media proposed
- The porous medium can have heterogeneous and spatially correlated pore/throat sizes
- Bubble statistics evolved with a population balance equation subject to apt closure
- Theory systematically validated against an existing pore network model for ripening
- Limitations and paths for future extensions are highlighted and discussed

Nicolas Bueno: Methodology, Formal Analysis, Writing - Original Draft

Luis Ayala: Methodology, Funding acquisition, Writing - Review & Editing,

Yashar Mehmani: Conceptualization, Methodology, Funding acquisition, Writing - Original Draft

Declaration of interests

☒ The authors declare that they have no known competing financial interests or personal relationships that could have appeared to influence the work reported in this paper.

☐ The authors declare the following financial interests/personal relationships which may be considered as potential competing interests: